energies

MDPI

Article

System-Level Assessment Methodology for PV–AEL–H_2–PEMFC Power-to-Power Systems: Constant-Efficiency Versus Quasi-Dynamic Modeling

Andrés Villarruel-Jaramillo [1,*], Freddy Nieto [1,2], Ignacio Arias [2,3], José M. Cardemil [2,3], Kenny Escobar-Segovia [4], Edgar Cando [1] and Salvatore Reina [1]

[1] Departamento de Ingeniería Mecánica, Escuela Politécnica Nacional, Quito 170517, Ecuador; freddy.nieto@epn.edu.ec (F.N.); edgar.cando@epn.edu.ec (E.C.); salvatore.reina@epn.edu.ec (S.R.)
[2] Departamento de Ingeniería Mecánica y Metalúrgica, Escuela de Ingeniería, Pontificia Universidad Católica de Chile, Vicuña Mackenna, Santiago 4860, Chile; ivarias@uc.cl (I.A.); jmcardem@uc.cl (J.M.C.)
[3] Solar Energy Research Center, SERC-Chile, Santiago 7820436, Chile
[4] Facultad de Ingeniería en Ciencias de la Tierra, RIIAHE, Escuela Superior Politécnica del Litoral, ESPOL, Campus Gustavo Galindo, Km. 30.5 Vía Perimetral, Guayaquil 090902, Ecuador; kescobar@espol.edu.ec
* Correspondence: andres.villarruel@epn.edu.ec

Abstract

Hydrogen-based power-to-power (PTP) systems complement batteries for long-duration storage, but their assessment often assumes fixed electrolyzer and fuel-cell efficiencies. The main innovation of this work is developing a system-level methodology to quantify how component-model fidelity affects the annual assessment of photovoltaic-alkaline electrolyzer-hydrogen-proton exchange membrane fuel cell systems. To highlight parameter and operational differences, two approaches are compared for the Santa Cruz–Baltra case study. Case A relies on simplified parameter assumptions, using fixed AEL and PEMFC efficiencies of 0.65 and 0.52. In contrast, Case B resolves operational differences by capturing operating-point-dependent electrochemical behavior, part-load variations, and AEL thermal-state propagation. Both cases use identical system boundaries and supervisory control, allowing model-fidelity effects on hydrogen production, storage utilization, and electricity recovery to be quantified. Annual simulations show that Case A predicts higher recovered electricity than Case B. For a representative configuration, global efficiency decreases from 0.529 to 0.440 (a 17% relative difference). The largest relative difference in recovered electricity (~91%) occurs in constrained configurations. Component-level experimental validation does not constitute full system-level validation. Overall, operating-point-dependent models materially alter annual PTP performance estimates under variable renewable operation.

Keywords: solar energy; green hydrogen; fuel cells; alkaline electrolyzer; power-to-power

Check for updates

Academic Editor: Adrian Ilinca

Received: 3 August 2026
Revised: 14 September 2026
Accepted: 16 September 2026
Published: 28 October 2026

Copyright: © 2026 by the authors. Licensee MDPI, Basel, Switzerland. This article is an open access article distributed under the terms and conditions of the Creative Commons Attribution (CC BY) license.

1. Introduction

The decarbonization of electricity systems requires storage technologies capable of absorbing variable renewable generation and delivering energy when generation and demand are temporally decoupled. Lithium-ion batteries are widely used for short-duration storage, power smoothing, and fast balancing in photovoltaic systems [1–4]. However, scaling up renewable electricity systems may also require storage technologies that complement batteries when energy must be stored over longer durations. Recent studies on hybrid battery–hydrogen systems have shown that batteries can manage short-term fluctuations,

whereas hydrogen can provide longer-duration or seasonal energy storage and subsequent electricity recovery through fuel cells [5]. In this context, hydrogen-based power-to-power (PTP) systems constitute a relevant long-duration storage pathway, in which surplus renewable electricity is converted into hydrogen (H_2) through electrolysis, stored—typically as compressed gas—and subsequently reconverted into electricity using a fuel cell [6–8].

A typical PV-driven PTP configuration integrates a PV generator, an electrolyzer, compressed H_2 storage, and a fuel cell. This architecture has been widely considered in energy planning, microgrid design, and techno-economic assessment studies because it provides temporal flexibility and allows renewable electricity to be stored as a chemical energy carrier [8–13]. Related optimization and techno-economic studies have also examined renewable hydrogen production for islands, mobility, industrial supply chains, and energy [14–24]. Although many of these studies do not include electricity reconversion, the reviewed studies illustrate the widespread use of aggregated electrolyzer representations in system-level assessments. These studies are valuable for defining capacities, costs, infrastructure requirements, and deployment scenarios. Nevertheless, the corresponding system-level formulations frequently represent the electrolyzer and fuel cell as aggregated conversion units using nominal efficiencies, fixed specific electricity consumption, or simplified input–output relationships.

The same modeling issue appears in the reconversion stage. Proton exchange membrane fuel cells (PEMFCs) exhibit nonlinear voltage–current behavior governed by thermodynamic equilibrium, activation overpotential, ohmic losses, concentration losses, reactant partial pressures, temperature, and membrane properties [25–28]. Consequently, the H_2 consumption, electrical output, and efficiency of a fuel cell cannot be fully represented by a single constant efficiency when the PTP system is evaluated under chronological renewable operation. Since errors in H_2 production propagate into storage state, fuel-cell dispatch, recovered electricity, and round-trip performance, component-level models become relevant for evaluating PTP configurations beyond nominal design points [8,9]. This simplification is relevant because water electrolyzers and fuel cells are thermoelectrochemical devices with nonlinear operating behavior. In alkaline electrolysis, the cell voltage, Faraday efficiency, H_2 production rate, operating temperature, and specific electricity consumption depend on current density, activation losses, ohmic losses, heat transfer, and operating conditions [29–32]. Therefore, assuming a constant electrolyzer efficiency, for example 60% on a lower-heating-value basis, can be useful for preliminary techno-economic screening but may distort H_2 production estimates when the electrolyzer operates under variable PV power and partial-load conditions. For the technologies, efficiency curves, and renewable-generation conditions examined in [33], neglecting part-load efficiency variations resulted in an overestimation of hydrogen production ranging from 5% to 24%. Similarly, reviews on PV-electrolyzer integration highlight that intermittent solar operation introduces additional constraints associated with dynamic response, temperature, pressure, and coupling strategy [34].

Despite the availability of variable-efficiency and low-order electrochemical models, limited system-level evidence is available on how replacing fixed AEL and PEMFC efficiencies with coupled model-based representations affects annual performance estimates across a common PV and hydrogen-storage design space. Techno-economic models are useful for deployment scenarios, but they may overlook the nonlinear response of commercial equipment under variable renewable input. Low-order electrochemical models can reproduce key operating trends, but their use in engineering screening requires a transparent procedure for linking model outputs with catalog-based nominal capacities. Therefore, this study proposes a methodology to evaluate commercial AELs and PEM fuel-cell systems coupled to PV generation using validated numerical models. The main contribution of this work

is a common temporal assessment framework for comparing two component-modeling approaches: a fixed-efficiency baseline and a model-based representation in which AEL and PEMFC performance depends on the operating point. Enabling the comparison of different PTP configurations through indicators such as instantaneous H_2 production, annual H_2 yield, specific electricity consumption, part-load operation, H_2 storage utilization, electricity reconversion, and overall PTP efficiency.

2. Literature Review

2.1. Alkaline Electrolysis and Stationary PEM Fuel-Cell Systems

Alkaline water electrolysis is one of the most mature technologies for renewable H_2 production because of its relatively low capital cost, commercial availability, and suitability for medium- and large-scale operation. Component representations used in system-level studies can be classified into several levels of fidelity: constant-efficiency or constant-specific-consumption models; load-dependent efficiency curves or piecewise input–output maps; steady-state electrochemical models evaluated at successive operating points; quasi-dynamic models with one or more propagated states; and fully dynamic models that resolve electrochemical, thermal, fluid, or control transients.

The appropriate level of model fidelity depends on the purpose and temporal scope of the analysis. Constant-efficiency and piecewise input–output representations are particularly suitable for preliminary screening, energy-planning, capacity-expansion, and large multi-scenario optimization studies, where limited data requirements and computational tractability are important. Steady-state electrochemical models are appropriate when part-load conversion behavior must be represented but state dynamics are not central to the analysis. Quasi-dynamic models are more suitable for chronological operation studies in which one or more slowly varying states, such as stack temperature, influence conversion performance between simulation steps. Fully dynamic models are required when fast electrochemical, thermal, fluid, pressure, start-up, shut-down, or control transients are themselves quantities of interest. In techno-economic and energy-planning studies, electrolyzers are therefore commonly represented through nominal power, minimum-load constraints, specific electricity consumption, H_2 production rate, and constant electricity-to-H_2 efficiency [14,17]. The widespread use of these simplified representations is largely motivated by their limited data requirements and low computational cost, which make them particularly convenient for optimization problems involving long time horizons, multiple locations, multiple scenarios, and investment decisions [15,22]. However, no universal error range can be assigned to a given model-fidelity level because the resulting deviation depends on the technology, parameterization, operating range, temporal resolution, control strategy, and performance metric considered.

However, alkaline electrolysis involves coupled electrochemical and thermal phenomena, and its operating performance varies with current density and temperature. Cell voltage is determined by the reversible potential and the associated activation and ohmic losses, whereas the H_2 production rate depends on the applied current and Faradaic efficiency. These quantities jointly determine the specific electricity consumption, while gas evolution and heat transfer influence the electrolyzer thermal state. Consequently, a fixed-efficiency representation may not capture the relevant operating variations when the electrolyzer is subjected to variable renewable input and frequent part-load operation.

For system-level applications, Ulleberg developed a low-order semi-empirical AEL formulation that combines thermodynamic relations, algebraic voltage–current behavior, Faradaic efficiency, and a lumped dynamic thermal balance [29]. The formulation was subsequently implemented in TRNSYS as Type 160, allowing the electrolyzer temperature to evolve between simulation steps while the electrochemical variables are recalculated

at each operating point [30]. This intermediate modeling approach has been applied to chronological PV-driven H_2 production and storage simulations, in which electrolyzer operation is coupled to the renewable electricity available over time [31].

At the cell level, AEL models can also be used to examine design–operation trade-offs. For example, optimization studies have shown that current density influences both capital- and operating-related performance: increasing the current density can reduce the active area required for a given production capacity, but it also increases cell voltage and specific electricity consumption [35]. This trade-off cannot be represented explicitly by a single fixed conversion efficiency. Accordingly, voltage–current and Faradaic-production relations provide a more suitable basis for evaluating how operating point, nominal capacity, and assumed operating limits affect electrolyzer performance. When these relations are combined with catalog-based nominal data, the resulting representation should be interpreted as the commercial-scale adaptation of a common reference model rather than as a unit-specific reproduction of each manufacturer's stack behavior.

PEM fuel cells used for stationary electricity generation present a similar modeling hierarchy. In system-level studies, PEMFC units are often represented as aggregated H_2-to-electricity converters activated during power-deficit periods. PEMFC behavior is usually described through nominal power, H_2 consumption, electrical efficiency, and storage constraints [5,10,11]. This representation is useful for microgrid sizing and long-term techno-economic optimization because of its low parameter requirements and computational simplicity, but it neglects the nonlinear electrochemical behavior of the cell.

Detailed PEMFC models describe the voltage–current curve as the result of reversible potential and irreversible losses. The Amphlett–Mann formulation is one of the most widely used semi-empirical approaches for PEMFC performance prediction, because it relates the cell voltage to thermodynamic equilibrium, activation overpotential, ohmic losses, concentration losses, partial pressures, temperature, membrane properties, and current density [25,26]. Correa et al. extended the use of electrochemical PEMFC models for electrical engineering applications, showing their suitability for system-level simulation and automation studies [27]. General fuel-cell theory also shows that the operating efficiency of PEMFC systems varies with current density and load, which directly affects H_2 consumption and recovered electricity [28].

Consequently, both AELs and PEM fuel cells exhibit nonlinear operating behavior. This is particularly relevant in PTP systems, where differences in H_2 production propagate into storage inventory, fuel-cell dispatch, recovered electricity, and round-trip efficiency. Low-order electrochemical models therefore provide an intermediate level of fidelity between fixed-efficiency representations and fully dynamic component models, while remaining sufficiently tractable for integration into chronological renewable-energy simulations. In the present study, this modeling level is used to assess how operating-point-dependent component behavior affects annual PV–H_2–PEMFC system performance relative to constant-efficiency representations.

This makes them suitable for evaluating commercial AELs and stationary PEMFC systems under realistic PV-driven operation.

2.2. Assessment of Photovoltaic Power-to-Power Systems

H_2-based PTP systems convert surplus renewable electricity into H_2, store it as a chemical energy carrier, and reconvert it into electricity when required. In PV-driven configurations, the main components are the PV generator, electrolyzer, H_2 compressor, compressed H_2 storage, and fuel cell. Compared with battery-only storage, this architecture decouples power capacity from energy storage capacity, making it attractive for long-duration storage, seasonal shifting, and high-renewable systems [5,8,9].

Several studies have assessed H_2 as a complement to batteries in renewable and islanded energy systems. Superchi et al. analyzed a hybrid battery–H_2 PTP configuration for Tilos, including wind and PV generation, BESS, an AEL, compressed H_2 storage, and a PEMFC. The hybrid configuration reduced the required PV and battery capacities while enabling full self-sufficiency and achieving a lower Levelized Cost Of Required Energy (LCORE) than the BESS-only case [5]. Similarly, Trapani et al. showed that H_2–battery storage can avoid the excessive oversizing of renewable generators and batteries in remote Norwegian islands, while Williams and Wang evaluated H_2 generation and compressed storage as part of a distributed renewable system for the Isle of Rum [10,11]. These studies support the role of H_2 in long-duration balancing, although the electrolyzer and fuel-cell subsystems are generally represented through aggregated efficiencies, operating ranges, and storage constraints rather than electrochemical models.

A second group of studies focuses on renewable H_2 production without complete PTP reconversion. Hajjaji and Cristofari evaluated a PV-driven H_2 refueling station in Ajaccio, where AELs were modeled using a constant efficiency and a specific electricity consumption of 50 kWh/kgH_2 to estimate PV capacity, electrolyzer capacity, and H_2 production [22]. Nami et al. optimized large-scale AEL deployment in Lolland–Falster under renewable surplus and transmission constraints, reporting optimal electrolyzer capacities of 1300 and 1700 MW for different transmission limits [17]. Similar simplified formulations are used in H_2 mobility and supply-chain studies for Corsica, Crete, and the Balearic Islands, where electrolyzer operation is mainly described through capacity, utilization, constant efficiency, or specific electricity consumption [14–16,36].

Other studies include H_2 reconversion or fuel-cell operation within broader hybrid systems. He et al. evaluated PV–wind–BESS systems with alkaline seawater electrolysis, compressed H_2 storage, and fuel cells for remote Japanese islands, using fixed conversion efficiencies for the H_2 subsystem [37]. Gao et al. proposed a H_2-based island integrated energy system, where H_2 storage and reconversion improve renewable utilization and energy self-sufficiency under uncertainty [38]. At larger scales, H_2 has also been modeled as a decarbonization, export, or sector-coupling vector in the Canary Archipelago, the Faroe Islands, and Shetland [20,21,23,24]. These works are valuable for strategic planning, but they are not focused on the detailed operational assessment of commercial AEL–PEMFC combinations under PV-driven PTP operation.

Overall, previous PV–H_2 and PTP studies commonly represent electrolyzers and fuel cells through constant efficiencies, specific electricity consumption, capacity limits, and dispatch rules [5,10,17,22,36,37]. This approach is suitable for system sizing and techno-economic screening, but it can simplify the part-load response of AELs and PEMFCs under variable renewable operation. Table 1 summarizes the main modeling assumptions identified in the reviewed studies, with emphasis on the conversion pathway, renewable energy source, electrolyzer technology, fuel-cell or reconversion unit, and the way in which electrolyzer and fuel-cell efficiencies are represented. The comparison shows that fixed-efficiency assumptions remain common, whereas only a smaller group of studies incorporates variable, part-load, electrochemical, or dynamic efficiency behavior.

This simplification is relevant because AEL efficiency defines the amount of H_2 produced from a given PV surplus, while PEMFC efficiency defines the electricity recovered from stored H_2. These two efficiencies directly affect H_2 storage availability, fuel-cell operating hours, effective capacity factor, recovered electricity, and consequently the LCOE of the PTP system [25–29]. Therefore, incorporating variable-efficiency behavior is necessary to obtain a more representative numerical approximation of PV-driven PTP operation.

Table 1. Summary of modeling assumptions in PV–H_2 and PTP studies.

Location	Route	Energy Source for H_2	Electrolyzer Type	η_{EL} Const.	Reported η_{EL} or SEC	Fuel Cell/Reconversion Type	η_{FC} Const.	η_{FC}/H_2 Use	Ref.
Greece, Tilos island	PTP	Wind + PV	AEL	×	59.8% LHV	PEMFC	×	50.8% LHV	[5]
Norway	PTP	Wind + PV	PEMEL	✓	58% LHV	PEMFC	✓	47% LHV	[10]
United Kingdom, Isle of Rum	PTP partial	Hydro + wind + PV	PEMEL	NR	NR	Modified H_2 gen-set	NR	NR	[11]
Japan	PTP	PV + wind + BESS	Alkaline seawater electrolysis	✓	61.5%	FC, type NR	✓	40%	[37]
NR	PTP	PV + offshore wind + wave	Electrolysis/SHPS, type not fully specified	NR	NR	HPP, type NR	NR	NR	[38]
France, Ajaccio	PTH_2	PV	AEL	✓	80%	–	–	–	[22]
Turkey	PTH_2	PV	AEL, TRNSYS Type 160a	×	NR	–	–	–	[31]
Spain, Balearic Islands	PTH_2	PV + grid	PEMEL	NR	NR	–	–	–	[16]
France, Corsica	PTH_2	PV + wind + hydro + grid	PEMEL, AEL and SO evaluated	NR	NR	FCEV end-use	–	–	[14,15]
Denmark, Lolland–Falster	PTH_2	PV + onshore wind + offshore wind + grid	AEL/AEC	NR	NR	–	–	–	[17]
Egypt	PTH_2	PV + wind	AEL electrochemical model	×	7.69–9.37%	–	–	–	[39]
Greece, Crete	PTH_2	Wind + grid/net metering	ELZ generic	NR	NR	FCEV end-use	–	–	[36]
Faroe Islands	PTH_2	Offshore wind	AEL, PEMEL, SOEC	✓	66%; 62%; 79%	–	–	–	[23]
Spain, Canary Islands	PTH_2	PV + wind; nuclear VHTR scenario	PEMEL and SOEC	✓	70.5%; 83.5%	–	–	–	[20]
Spain, Canary Islands	PTH_2 + electricity	PV + wind + SMR	PEMEL and SOEC	NR	NR	–	–	–	[21]
United Kingdom, Shetland	PTH_2	Offshore wind + onshore wind + wave + PV	WEL generic	✓	72%	–	–	–	[24]
Spain, Formentera	PTP	PV + wind	PEM electrolyser	✓	68%	PEMFC/RHFC	✓	46%	[40]
Italy, Ginostra–Stromboli	PTP	PV	EL, modeled through PWA efficiency curve	×	NR	FC, modeled through PWA efficiency curve	×	NR	[41]
Norway, Froan islands	PTP	PV + wind	PEMEL	×	NR	PEMFC	×	NR	[42]
Iraq, Baghdad	PTH_2	Off-grid PV	PEMEL	✓	>95%	–	–	–	[43]
China, Northwest China	PTP + PTH_2 export	PV + wind	AEL, 15 MW class	×	NR	PEMFC	NR	NR	[44]
NR	PTP + PTH_2	PV + grid support	PEMEL	✓	60–80%	PEMFC	✓	60%	[45]

Note: PTP = Power-to-Power; PTH_2 = Power-to-Hydrogen; NR = not reported; SEC = specific electricity consumption; EL = electrolyzer; FC = fuel cell; AEL = alkaline electrolyzer; PEMEL = proton-exchange membrane electrolyzer; PEMFC = proton-exchange membrane fuel cell; RHFC = regenerative hydrogen fuel cell; RES = renewable energy sources; BESS = battery energy storage system. The symbol ✓ indicates a constant or fixed efficiency assumption, whereas × indicates variable, part-load, electrochemical, or dynamic efficiency behavior.

2.3. Research Gap and Objective

Previous PV–H_2 and PTP studies commonly represent electrolyzers and fuel cells using constant efficiencies, fixed SEC values, nominal capacities, and dispatch rules. Although this approach is useful for preliminary sizing and techno-economic screening, it can obscure the nonlinear part-load response of AELs and PEMFCs under temporal PV operation. This is relevant because AEL performance determines the conversion of PV surplus into H_2, while PEMFC performance determines the electricity recovered from stored H_2. Therefore, simplified component assumptions can propagate through the PTP chain and affect H_2 production, storage utilization, fuel-cell dispatch, recovered electricity, η_{PTP}, and subsequent levelized cost indicators.

The research gap addressed in this work is the limited quantitative evidence on how constant-efficiency assumptions affect the operational assessment of commercial PV–AEL–H_2–PEMFC systems. Although validated low-order AEL and PEMFC models are available in the literature, their integration with commercial equipment data and temporal PV-driven PTP simulations remains limited. Consequently, it is still necessary to quantify how replacing fixed efficiencies with quasi-dynamic component models modifies the relationship between PV field area, H_2 storage duration, *SF*, η_{PTP}, and E_{PEMFC}.

Accordingly, this study develops and applies a validated model-based methodology to assess commercial AEL and PEMFC systems coupled to PV generation in a PTP configuration. The proposed framework validates the AEL and PEMFC models, scales them to commercial equipment capacities, integrates them with a 6 min temporal PV and demand simulation, and compares a constant-efficiency baseline against a quasi-dynamic model-based configuration. The comparison focuses on *SF*, η_{PTP}, E_{PEMFC}, $RD_{\eta_{PTP}}$, and $RD_{E_{PEMFC}}$ to determine whether fixed-efficiency assumptions are sufficient for commercial PTP assessment or whether quasi-dynamic models are required to obtain a more representative estimate of electricity recovery.

3. Methodology

3.1. Case Study and Electric Demand Profile

The case study corresponds to the Santa Cruz electricity demand in the Galápagos Islands, Ecuador, with Baltra considered as a technically feasible site for PV-driven H_2 production. This configuration provides an isolated-island context for evaluating future PTP integration scenarios, particularly because electricity supply in the Galápagos has historically depended on diesel-fired thermoelectric generation [46]. The 2025 annual demand and target peak demand were defined from the Galápagos Energy Transition Plan [47]. Measured subhourly electricity demand data for Santa Cruz–Baltra are not publicly available; therefore, a synthetic temporal demand profile was generated. Monthly demand allocation was based on the empirical demand model proposed by Córdova for the Galápagos electricity system [48]. The Córdova equation is not reproduced here because it is used only as an external reference for monthly demand allocation. The main input data used to generate the Santa Cruz–Baltra demand profile are summarized in Table 2.

Table 2. Input parameters used to generate the Santa Cruz–Baltra electric demand profile [47].

Location	T_{amb}	E_{year}	E_{month}	P_{target}	P_{24h}
Santa Cruz–Baltra	NSRDB	41.99 GWh	Córdova-based allocation	7.51 MW	Local representative profile

The synthetic demand model used the subhourly ambient-temperature time series (T_{amb}) to modulate the temporal load profile, the monthly electricity consumption E_{month}, the target peak demand P_{target}, and the normalized 24 h demand profile P_{24h}. The output

time step was fixed at 6 min, corresponding to 0.1 h, to provide the subhourly resolution required by the quasi-dynamic AEL and PEMFC models, remain close to the available 10 min NREL meteorological records, and avoid the additional computational cost of finer resolutions such as 1 min. The effect of ambient temperature was represented through a cooling degree indicator,

$$CDD_d = \max\left(0, \overline{T}_{\mathrm{amb},d} - 18\right) \tag{1}$$

where CDD_d is the cooling degree indicator for day d [°C], and $\overline{T}_{\mathrm{amb},d}$ is the daily mean ambient temperature [°C]. For each month m, the preliminary daily electricity consumption was calculated as

$$E_d^{\mathrm{raw}} = \frac{E_{\mathrm{month},m}}{N_m} \frac{f_{\mathrm{dow},d}}{\overline{f}_{\mathrm{dow},m}} \left[1 + 0.02\left(CDD_d - \overline{CDD}_m\right)\right](1 + \varepsilon_d) \tag{2}$$

where E_d^{raw} is the preliminary daily electricity consumption [kWh], $E_{month,m}$ is the monthly electricity consumption assigned to month m [kWh], N_m is the number of days in month m [days], $f_{\mathrm{dow},d}$ is the day-of-week factor, $\overline{f}_{\mathrm{dow},m}$ is its monthly mean value, $\overline{CDD}_m$ is the monthly mean value of CDD_d, and ε_d is the daily stochastic component. The stochastic term was generated as $\varepsilon_d = 0.90\varepsilon_{d-1} + 0.02\xi_d$, where ξ_d is a normally distributed random variable. The preliminary daily values were rescaled as $E_d = E_d^{\mathrm{raw}} E_{\mathrm{month},m} / \sum_{j \in \mathcal{D}_m} E_j^{\mathrm{raw}}$, where E_d is the corrected daily electricity consumption and $\mathcal{D}_m$ is the set of days belonging to month m. This correction enforces $\sum_{d \in \mathcal{D}_m} E_d = E_{\mathrm{month},m}$. The 24 h demand profile was used only as a normalized shape input, with $p_r = P_{24,r} / \sum_{q=1}^{24} P_{24,q}$, where p_r is the normalized demand fraction at hour r. The hourly shape was interpolated to the 6 min time step using a shape-preserving piecewise cubic Hermite interpolation method, which preserves the monotonic behavior of the original hourly profile and avoids artificial oscillations between consecutive demand points [49]. The resulting subhourly profile was normalized as $s_i = \tilde{p}_i / \sum_{k=1}^{N_{\mathrm{step}}} \tilde{p}_k$, where $\tilde{p}_i$ is the interpolated value at time step i, s_i is the base subhourly demand fraction, and N_{step} is the number of time steps per day. The base subhourly shape was then corrected using the daily temperature condition and a subdaily stochastic component:

$$S_{i,d}^{\mathrm{raw}} = s_i \exp\left[0.06\left(\frac{t_i - 18}{12}\right)\left(CDD_d - \widetilde{CDD}\right)\right] \max\left(0.05, 1 + \eta_{i,d}\right) \tag{3}$$

where $S_{i,d}^{\mathrm{raw}}$ is the preliminary subhourly demand shape, t_i is the hour of the day, $\widetilde{CDD}$ is the median value of CDD_d, and $\eta_{i,d}$ is the subdaily stochastic component. This component was generated as $\eta_{i,d} = 0.90\eta_{i-1,d} + 0.02\zeta_{i,d}$, where $\zeta_{i,d}$ is a normally distributed random variable. The corrected subhourly shape was normalized as $S_{i,d} = S_{i,d}^{\mathrm{raw}} / \sum_{k=1}^{N_{\mathrm{step}}} S_{k,d}^{\mathrm{raw}}$. To match the target peak demand, the normalized shape was modified using the exponent γ:

$$S_{i,d}^{\gamma} = \frac{\left(S_{i,d}\right)^{\gamma}}{\sum_{k=1}^{N_{\mathrm{step}}} \left(S_{k,d}\right)^{\gamma}} \tag{4}$$

where $S_{i,d}^{\gamma}$ is the peak-adjusted subhourly demand fraction. The value of γ was obtained iteratively until $\max_{i,d}\left(E_d S_{i,d}^{\gamma} / dt_{\mathrm{out,h}}\right) = P_{\mathrm{target}}$, where $dt_{\mathrm{out,h}}$ is the output time step expressed in hours. The final temporal demand profile was then calculated as

$$P_{i,d} = \frac{E_d S_{i,d}^{\gamma}}{dt_{\mathrm{out,h}}} \tag{5}$$

where $P_{i,d}$ is the electric demand at time step i of day d [kW], E_d is the corrected daily electricity consumption [kWh], and $dt_{out,h}$ is the output time step expressed in hours [h]. Consequently, the generated profile should be interpreted as a representative temporal boundary condition rather than as a measured load record. Its representativeness is constrained by the projected annual demand, the target peak demand, the monthly allocation,

the normalized 24 h demand shape, and the ambient-temperature modulation. The monthly rescaling enforces the prescribed monthly energy, while the exponent correction adjusts the annual maximum demand to the target peak value. Therefore, the profile preserves the main annual, seasonal, daily, and peak-demand constraints required for the comparative PTP assessment, although it does not reproduce feeder-level measured demand fluctuations.

3.2. Solar Resource and PV Generation Model

The solar-resource characterization was performed for Baltra, Galápagos, which was adopted as the reference location for PV generation in the Santa Cruz–Baltra case study. Satellite-derived meteorological data were obtained from the National Solar Radiation Database (NSRDB), including global horizontal irradiance (GHI), direct normal irradiance (DNI), diffuse horizontal irradiance (DHI), ambient temperature T_{amb}, wind speed, pressure, and relative humidity [50]. The synthetic demand profile was generated directly at a 6 min resolution, whereas the original NSRDB meteorological records were temporally processed and resampled to the same computational grid to synchronize the PV-generation calculation with the coupled PTP simulation. This common grid is used for the supervisory control, H_2 inventory, and component-state calculations. This resampling is not intended to reconstruct meteorological fluctuations below the temporal resolution of the original NSRDB data and therefore does not create additional physical information on sub-interval solar variability. Rather, the 6 min interval defines the numerical integration and state-update grid of the coupled PTP model. This distinction is relevant for the quasi-dynamic AEL formulation because the thermal state is propagated chronologically between successive operating points, while the electrochemical operating point, H_2 production, storage balance, and supervisory decisions are updated at each simulation step [29,34]. Previous assessments of renewable-driven electrolysis have shown that temporal aggregation can affect calculated H_2 production, although its influence may be smaller than that associated with neglecting load-dependent electrolyzer efficiency. For example, hourly renewable data produced differences of approximately 0.2–2% relative to 5 min data in the cases analyzed by Virah-Sawmy et al. [33]. Consequently, the 6 min grid is adopted here as a common chronological simulation interval rather than as a claim of 6 min meteorological fidelity. Only the solar and meteorological variables required by the PV generation model were retained. The horizontal irradiance components were transposed to the tilted PV plane using the HDKR model, following the tilted-surface radiation formulation described by Duffie and Beckman [51]. The surface tilt was set equal to the local latitude, the albedo was fixed at 0.2, and the surface orientation was defined for the Southern Hemisphere. This treatment provides the effective irradiance input required to simulate the PV module under temporal irradiance and temperature conditions. Figure 1 summarizes the solar-resource characterization used for the Baltra PV model, including the geographical location, annual GHI, daily GHI series, and daily mean ambient temperature. The annual GHI at Baltra is 1979 kWh/m^2, confirming the suitability of the site for evaluating PV-driven H_2 production under island conditions. This representation was adopted instead of a clearness-index scatter plot because the present study focuses on the operational effect of variable PV input on AEL and PEMFC performance rather than on a detailed atmospheric classification of the solar resource.

The PV field was simulated using PVLib-based routines. The module output was calculated from the effective irradiance, operating cell temperature, and the five-parameter single-diode model corrected under operating conditions. Cell temperature was estimated using the Sandia temperature model, while DC/AC conversion was represented using the Sandia inverter model [52–54]. These models were used as implemented reference formulations; therefore, their governing equations are not repeated here. The PV module

was selected from the CEC/SAM module library [55]. The selected module corresponds to a mono-crystalline silicon technology with a nominal power of 445.12 W and a reference efficiency of 23.80%. The main technical parameters used in the PV simulation are summarized in Table A1. The inverter was selected from the CEC/SAM inverter database using the same PVLib simulation environment. The selection retained high-power candidates with an adequate MPPT voltage window for the series-parallel PV configuration and used the Sandia inverter model to convert the simulated DC PV output into AC power. The resulting temporal AC PV generation profile was then used as the renewable electricity input for the PTP simulation. Thus, the PV model provides a time-dependent generation signal that preserves irradiance intermittency, temperature effects, and inverter conversion losses without introducing additional empirical PV equations in the present work.

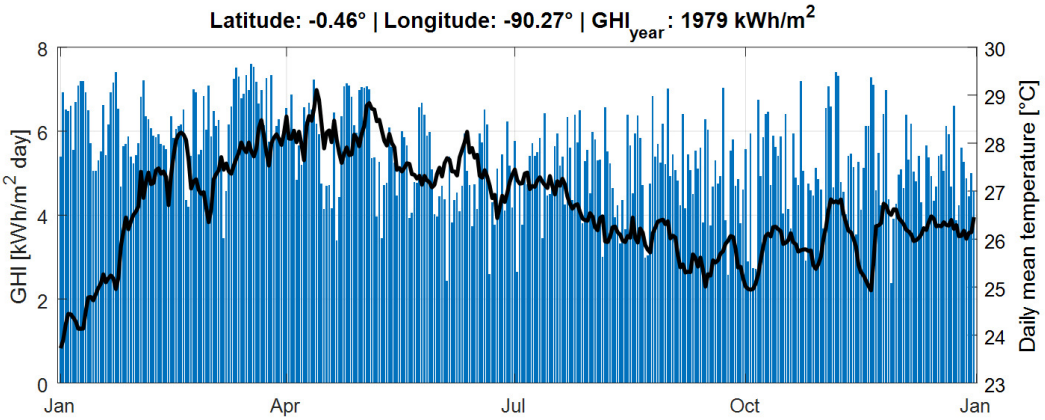


Figure 1. Solar-resource characterization for the Baltra, Galapagos, Ecuador PV model: geographical location, annual GHI, daily GHI (blue bars), and daily mean ambient temperature (black line).

3.3. Constant-Efficiency and Quasi-Dynamic Model Configurations

Two PTP model configurations were evaluated to quantify the effect of using constant-efficiency assumptions instead of quasi-dynamic electrochemical component models. Case A represents the simplified constant-efficiency baseline commonly used in system-level studies, where both the AEL and the PEMFC are modeled using fixed lower-heating-value efficiencies. Case B represents the proposed quasi-dynamic configuration, where the AEL is simulated using the electrochemical and thermal formulation described in Section 3.4, and the PEMFC is simulated using the generalized Amphlett–Mann formulation described in Section 3.5. The constant-efficiency representations used in Case A bypass the voltage–current relations, Faraday efficiency, thermal response, activation losses, ohmic losses, concentration losses, and operating-point dependence included in the quasi-dynamic models. Therefore, Case A converts electrical energy into H_2, and stored H_2 back into electricity, using fixed proportional efficiencies. In contrast, Case B calculates H_2 production, H_2 consumption, recovered electricity, component efficiency, and heat generation as functions of the instantaneous electrochemical operating conditions. The two model configurations are summarized in Table 3. Both cases were evaluated using the same PV generation profile, electric demand profile, H_2 storage model, compressor model, sizing procedure, and supervisory control logic. Therefore, the differences between the cases are attributed to the representation of the AEL and PEMFC conversion behavior.

To compare the response surfaces obtained for both cases, a relative difference factor was calculated for each performance indicator. For a generic indicator X, the relative difference factor (RD_X) was defined as

$$RD_X = 100 \cdot \left(\frac{X_A - X_B}{X_A} \right) \tag{6}$$

where X_A and X_B are the values obtained for Case A and Case B, respectively. In this work, Equation (6) was applied to the annual PTP efficiency (η_{PTP}) and to the annual electricity recovered by the PEMFC (E_{PEMFC}) as used in the relative-difference maps. A positive value indicates that the constant-efficiency baseline predicts a higher value than the quasi-dynamic model, whereas a negative value indicates that the quasi-dynamic model predicts a higher value.

Table 3. Model configurations used to compare constant-efficiency and quasi-dynamic component representations.

Case	AEL Model	PEMFC Model	Purpose
A	Constant efficiency ($\eta_{AEL} = 0.65$) [56]	Constant efficiency ($\eta_{FC} = 0.52$) [57]	Simplified system-level baseline
B	Quasi-dynamic	Quasi-dynamic	Proposed model-based configuration

To distinguish the effect of the literature-based efficiency assumptions from the effect of suppressing the operating-point dependence of the electrochemical models, an additional sensitivity configuration, denoted Case A*, was evaluated. Case A* retained the same constant-efficiency formulation, system boundaries, supervisory control, and simulation time step as Case A; however, the fixed AEL and PEMFC efficiencies were replaced by annual energy-equivalent efficiencies obtained from Case B. Therefore, Case A* does not constitute an additional physical model but rather a controlled sensitivity case designed to determine whether the discrepancies between Cases A and B arise predominantly from the selected constant-efficiency values or from the loss of time-dependent electrochemical coupling. For the AEL, the annual energy-equivalent efficiency derived from Case B was calculated as

$$\eta^*_{AEL,B} = \frac{E_{H_2,B}}{E_{AEL,B}} = \frac{\sum_{k=1}^{N} \dot{n}^k_{H_2,B} LHV_{H_2,mol} \Delta t}{\sum_{k=1}^{N} P^k_{AEL,B} \Delta t} \tag{7}$$

where $E_{H_2,B}$ is the annual chemical energy of the hydrogen produced in Case B, $E_{AEL,B}$ is the annual electrical energy supplied to the AEL, $\dot{n}^k_{H_2,B}$ is the hydrogen molar production rate [mol s^{-1}], $LHV_{H_2,mol}$ is the molar lower heating value of hydrogen [J mol^{-1}], $P^k_{AEL,B}$ is the electrolyzer electrical input power [W], and Δt is the simulation time step [s].

Similarly, the annual energy-equivalent PEMFC efficiency was calculated as

$$\eta^*_{PEMFC,B} = \frac{E_{PEMFC,B}}{E_{H_2,PEMFC,B}} = \frac{\sum_{k=1}^{N} P^k_{PEMFC,B} \Delta t}{\sum_{k=1}^{N} \dot{n}^k_{H_2,PEMFC,B} LHV_{H_2,mol} \Delta t} \tag{8}$$

where $E_{PEMFC,B}$ is the annual electrical energy generated by the PEMFC, $E_{H_2,PEMFC,B}$ is the chemical energy of the hydrogen consumed by the PEMFC, $P^k_{PEMFC,B}$ is the PEMFC electrical output power [W], and $\dot{n}^k_{H_2,PEMFC,B}$ is the hydrogen molar consumption rate [mol s^{-1}]. These energy-equivalent efficiencies were subsequently imposed as constant values in the Case A formulation to generate Case A*. Unlike a simple arithmetic average of the instantaneous efficiencies, Equations (7) and (8) preserve the annual input–output energy conversion ratios predicted by Case B. Consequently, the comparison between Case A and Case A* quantifies the influence of the initially assumed literature-based constant efficiencies, whereas the comparison between Case A* and Case B isolates the residual effect associated with representing the conversion processes through constant efficiencies rather than operating-point-dependent electrochemical models.

3.4. AEL Model and Commercial Scaling

Following the configurations defined in Section 3.3, this subsection describes the AEL model used for the Power-to-Hydrogen (PTH_2) conversion stage and its commercial scaling. The quasi-dynamic formulation follows the alkaline-electrolyzer model reported in [29,30], which includes thermodynamic equilibrium, empirical voltage–current behavior, Faraday efficiency, and lumped thermal response. The overall electrolysis reaction is

$$H_2O(l) + \text{Electric energy} \rightarrow H_2(g) + \frac{1}{2}O_2(g) \tag{9}$$

For both formulations, the normal volumetric H_2 production rate of the AEL ($\dot{V}^k_{H_2,AEL}$) was obtained from the molar H_2 production rate ($\dot{n}^k_{H_2,AEL}$) as

$$\dot{V}^k_{H_2,AEL} = \frac{3600\dot{n}^k_{H_2,AEL}}{C_{STD}} \tag{10}$$

where C_{STD} is the molar concentration of an ideal gas at standard conditions [mol m^{-3}], $\dot{n}^k_{H_2,AEL}$ is the molar H_2 production rate [mol s^{-1}], and $\dot{V}^k_{H_2,AEL}$ is the normal volumetric H_2 production rate [Nm^3 h^{-1}]. The corresponding normal volumetric O_2 production rate of the AEL ($\dot{V}^k_{O_2,AEL}$) was calculated from the electrolysis stoichiometry as

$$\dot{V}^k_{O_2,AEL} = \frac{1}{2}\dot{V}^k_{H_2,AEL} \tag{11}$$

In the constant-efficiency formulation, the AEL was represented as a proportional electricity-to-H_2 conversion block. The molar H_2 production rate of the AEL ($\dot{n}^k_{H_2,AEL}$) was calculated using a fixed lower-heating-value efficiency ($\eta_{AEL,const}$):

$$\dot{n}^k_{H_2,AEL} = \frac{\eta_{AEL,const}P^k_{AEL}}{LHV_{H_2,mol}} \tag{12}$$

where P^k_{AEL} is the electrical power assigned to electrolysis [W] and $LHV_{H_2,mol}$ is the molar lower heating value of H_2 [J mol^{-1}]. In this case, the AEL efficiency is an input parameter and does not vary with current density, cell voltage, Faraday efficiency, or temperature.

For the quasi-dynamic formulation, the AEL cell voltage (U^k_{cell}) was calculated using the empirical voltage–current relation proposed for alkaline electrolysis [29,30]:

$$U^k_{cell} = U_{rev} + r'^{,k}\frac{I^k_{stack}}{A_e} + s'\log_{10}\left(t'^{,k}\frac{I^k_{stack}}{A_e} + 1\right) \tag{13}$$

where U_{rev} is the reversible voltage [V], I^k_{stack} is the stack current [A], A_e is the electrode area [m^2], and $r'^{,k}$, s', and $t'^{,k}$ are empirical voltage–current coefficients. The AEL current density used for reporting polarization curves (J_{AEL}) was calculated as $J_{AEL} = I^k_{stack}/(10^4 A_e)$, where J_{AEL} is expressed in A cm^{-2} when A_e is given in m^2. The temperature-dependent definitions of $r'^{,k}$, s', and $t'^{,k}$ follow the original quasi-dynamic AEL formulation [29,30]. The Faraday efficiency (η^k_F) was evaluated using the empirical correlation reported for the same AEL formulation:

$$\eta^k_F = \frac{a_2\left(i^k_{stack}\right)^2}{a_1 + \left(i^k_{stack}\right)^2} \tag{14}$$

where $i^k_{stack} = 1000J^k_{AEL}$ is the current density expressed in mA cm^{-2} for the Faraday-efficiency correlation, and a_1 and a_2 are empirical Faraday-efficiency coefficients. The molar H_2 production rate at stack level ($\dot{n}^k_{H_2,stack}$) was then calculated using Faraday's law:

$$\dot{n}^k_{H_2,stack} = \eta^k_F\frac{N_{cells}I^k_{stack}}{2F} \tag{15}$$

where N_{cells} is the number of cells connected in series and F is the Faraday constant [C mol^{-1}]. The stack voltage (U^k_{stack}) and stack electrical power (P^k_{stack}) were obtained as

$$U^k_{\text{stack}} = N_{\text{cells}} U^k_{\text{cell}}, \qquad P^k_{\text{stack}} = U^k_{\text{stack}} I^k_{\text{stack}} \tag{16}$$

where U^k_{stack} is the AEL stack voltage [V] and P^k_{stack} is the stack electrical power [W] at time step k. The voltage-based electrical efficiency (η^k_{e}) and total AEL efficiency (η^k_{ely}) were computed as

$$\eta^k_{\text{e}} = \frac{U_{\text{tn}}}{U^k_{\text{cell}}}, \qquad \eta^k_{\text{ely}} = \eta^k_{\text{e}} \eta^k_{\text{F}} \tag{17}$$

where U_{tn} is the thermoneutral voltage [V]. Therefore, unlike the constant-efficiency representation, the quasi-dynamic formulation calculates η^k_{ely} as an output of the electrochemical operating point. The specific electricity consumption of the AEL (SEC_{AEL}) is calculated from the annual electrical energy consumed by the electrolyzer and the corresponding annual H_2 production as

$$SEC_{\text{AEL}} = \frac{E_{\text{AEL}}}{m_{\text{H}_2,\text{year}}} \tag{18}$$

where SEC_{AEL} is expressed in kWh $\text{kg}^{-1}_{\text{H}_2}$, E_{AEL} is the annual electrical energy consumed by the AEL [kWh], and $m_{\text{H}_2,\text{year}}$ is the annual H_2 production [kg]. The thermal response of the electrolyzer was represented using the lumped thermal balance reported in [29,30]; its role is to update the AEL temperature and, consequently, the voltage–current response during the annual simulation.

Regarding the temporal resolution, the 6-min simulation step is specifically used to numerically track the stack temperature transients during rapid PV power fluctuations. The model does not assume instantaneous thermal equilibration. Instead, the lumped thermal capacitance of the AEL stack inherently accounts for its thermal inertia. At each time step, the stack temperature is dynamically updated based on the energy balance between internal heat generation (caused by irreversible electrochemical losses) and heat dissipation to the environment or cooling system. This enables the model to capture the realistic heating and cooling dynamics that continuously alter the AEL polarization curve throughout the day.

To highlight the fundamental differences between both approaches, Table 4 summarizes how the main AEL variables are represented in each formulation.

Table 4. Comparison between the constant-efficiency and quasi-dynamic AEL formulations.

Modeling Aspect	Case A: Constant-Efficiency	Case B: Quasi-Dynamic
Model basis	Fixed electricity-to-H_2 conversion efficiency.	Quasi-dynamic alkaline-electrolyzer formulation [29,30].
Electrical input	Directly assigned as P^k_{AEL}.	Represented through stack current and voltage.
Efficiency treatment	Fixed scalar value, $\eta_{\text{AEL,const}}$.	Variable, calculated from voltage and Faraday efficiencies.
H_2 production	Direct proportional mapping using Equation (12).	Calculated from Faraday's law using Equation (15).
Gas production	H_2 and O_2 flows from Equations (10) and (11).	H_2 and O_2 flows from Equations (10) and (11) after stack-level scaling.
Voltage behavior	Not explicitly modeled.	Calculated using Equations (13) and (16).
Thermal behavior	Not resolved.	Included through the lumped thermal formulation of [29,30].
Main role	Baseline for system-level comparison.	Assessment of electrochemical and thermal effects under variable PV operation.

For commercial-scale integration, the catalog information was used to define the installed AEL capacity and to adapt the stack-level quasi-dynamic model to commercial equipment. The nominal AEL power (P_{nom}), nominal H_2 production rate ($\dot{V}_{\text{H}_2,\text{nom}}$), and nominal

outlet pressure (p_{nom}) were taken from commercial catalogues, while the literature-based electrochemical and thermal parameters used for commercial scaling followed the reference AEL formulation [29–31]. In the constant-efficiency formulation, the selected commercial capacity defines the maximum electrical input allowed for electrolysis, whereas H_2 production is calculated using the prescribed $\eta_{AEL,const}$. In the quasi-dynamic formulation, the same commercial information is used to determine the number of equivalent stacks required to reproduce the nominal commercial H_2 production capacity. The nominal stack current ($I_{stack,nom}$) was calculated from the nominal current density (i_{nom}) and electrode area (A_e) as

$$I_{stack,nom} = 10 i_{nom} A_e \tag{19}$$

where i_{nom} is expressed in mA cm^{-2} and A_e in m^2. The factor 10 accounts for the unit conversion from mA cm^{-2} to A m^{-2}. The nominal stack voltage ($U_{stack,nom}$) was obtained from Equation (16) evaluated at nominal conditions. The nominal H_2 production rate of one modeled stack ($\dot{V}_{H_2,stack,nom}$) was obtained from Equations (15) and (10) evaluated at $I_{stack,nom}$.

The number of equivalent series-connected AEL modules ($N_{ser,ely}$) was defined from the assumed DC bus voltage (V_{dc}) and nominal stack voltage ($U_{stack,nom}$) as

$$N_{ser,ely} = \max\left(1, \left\lceil \frac{V_{dc}}{U_{stack,nom}} \right\rceil\right) \tag{20}$$

The number of equivalent parallel branches ($N_{par,ely}$) required to reproduce the manufacturer H_2 production capacity was calculated from the nominal H_2 production rate of the commercial AEL ($\dot{V}_{H_2,nom}$), the number of equivalent series-connected modules ($N_{ser,ely}$), and the nominal H_2 production rate of one modeled stack ($\dot{V}_{H_2,stack,nom}$) as

$$N_{par,ely} = \left\lceil \frac{\dot{V}_{H_2,nom}}{N_{ser,ely}\dot{V}_{H_2,stack,nom}} \right\rceil \tag{21}$$

The total number of equivalent modeled stacks (N_{stacks}) was then obtained from the number of equivalent series-connected modules ($N_{ser,ely}$) and equivalent parallel branches ($N_{par,ely}$) as

$$N_{stacks} = N_{ser,ely} N_{par,ely} \tag{22}$$

For the quasi-dynamic formulation, the commercial-scale normal volumetric production rates of H_2 and O_2 ($\dot{V}^k_{H_2,AEL}$ and $\dot{V}^k_{O_2,AEL}$) were obtained by scaling the stack-level outputs ($\dot{V}^k_{H_2,stack}$ and $\dot{V}^k_{O_2,stack}$) with the total number of equivalent stacks (N_{stacks}) as

$$\dot{V}^k_{H_2,AEL} = N_{stacks}\dot{V}^k_{H_2,stack}, \qquad \dot{V}^k_{O_2,AEL} = N_{stacks}\dot{V}^k_{O_2,stack} \tag{23}$$

The commercial-scale AEL electrical power (P^k_{AEL}) was calculated from the stack electrical power (P^k_{stack}) and the total number of equivalent stacks (N_{stacks}) as

$$P^k_{AEL} = N_{stacks} P^k_{stack} \tag{24}$$

This definition keeps the same symbol, P^k_{AEL}, for the electrolyzer electrical input used by both the constant-efficiency and quasi-dynamic formulations. The nominal system current (I_{nom}) and the maximum current considered in the operating sweep (I_{max}) were bounded from the nominal AEL power (P_{nom}), assumed DC bus voltage (V_{dc}), and overload margin (γ_I) as

$$I_{nom} = \frac{P_{nom}}{V_{dc}}, \qquad I_{max} = \gamma_I I_{nom} \tag{25}$$

The commercial AEL capacities used as catalog-based inputs are summarized in Table 5, and the common literature-based and derived parameters used for commercial scaling are reported in Table A2.

Table 5. Commercial AEL capacities used as catalog-based input data.

Model	P_{nom}	$\dot{V}_{H_2,nom}$	p_{nom}	Catalog Source
A1-5	25 kW	5 Nm^3/h	–	[58]
A1-15	75 kW	15 Nm^3/h	–	[58]
A1-20	100 kW	20 Nm^3/h	–	[58]
A1-30	150 kW	30 Nm^3/h	–	[58]
A1-100	500 kW	100 Nm^3/h	–	[58]
AEL-1 MW	1 MW	200 Nm^3/h	1.6 MPa	[59]
AEL-5 MW	5 MW	1000 Nm^3/h	1.6 MPa	[59]
AEL-20 MW	20 MW	4000 Nm^3/h	1.6 MPa	[59]
AEL-100 MW	100 MW	20,000 Nm^3/h	1.6 MPa	[59]

3.5. Generalized Amphlett–Mann PEMFC Model and Commercial Scaling

The PEMFC model describes the H_2-to-electricity reconversion stage and its adaptation to commercial fuel-cell capacities. The quasi-dynamic formulation follows the generalized Amphlett–Mann PEMFC model [25,26], preserving the thermodynamic, activation, ohmic, and concentration-loss terms of the original formulation [27]. The overall cell voltage (V_{cell}) was calculated by subtracting the irreversible losses from the reversible thermodynamic voltage:

$$V_{cell} = E_{Nernst} - \eta_{act} - \eta_{ohmic} - \eta_{conc} \quad (26)$$

where E_{Nernst} is the Nernst voltage, evaluated as a function of the stack temperature T_{stack} [K] and reactant partial pressures p_{H_2} and p_{O_2} [bar]:

$$E_{Nernst} = 1.23 - 0.00085(T_{stack} - 298) + 0.0000431 T_{stack} \ln\left(p_{H_2} p_{O_2}^{0.5}\right) \quad (27)$$

The irreversible overpotentials (η_{act}, η_{ohmic}, and η_{conc}) are defined by the operating current density ($J_{PEMFC} = I/A_{PEMFC}$ [A cm^{-2}]), the oxygen concentration C_{O_2} [mol cm^{-3}], and empirical parameters:

$$\eta_{act} = -0.95 + 0.00243 T_{stack} - 0.000192 T_{stack} \ln(J_{PEMFC}) + 0.000076 T_{stack} \ln(C_{O_2}) \quad (28)$$

$$\eta_{ohmic} = -J t_{PEM} \frac{8}{\exp\left[3.6\left(1 - \frac{353}{T_{stack}}\right)\right]} \left(1 + 1.64J + \gamma_w J^3\right) \quad (29)$$

$$\eta_{conc} = -B \ln\left(1 - \frac{J}{J_{max}}\right) \quad (30)$$

The stack voltage (V_{stack}), electrical power (P_{stack}), and molar H_2 consumption rate ($\dot{n}_{H_2}$) are then scaled by the number of cells in series (N_{cells}):

$$V_{stack} = N_{cells} V_{cell}, \qquad P_{stack} = V_{stack} I, \qquad \dot{n}_{H_2} = \frac{N_{cells} I}{2F} \quad (31)$$

where V_{stack} is the stack voltage [V], P_{stack} is the electrical power [W], and $\dot{n}_{H_2}$ is the molar H_2 consumption rate [mol s^{-1}].

For the annual PTP simulations, the PEMFC was evaluated at an operating temperature of 65 °C and an effective cell pressure of 2.0 bar. Reactant availability was represented using hydrogen and air stoichiometric factors of $S_{H_2} = 1.3$ and $S_{air} = 2.5$, respectively [60]. The hydrogen and oxygen partial pressures entering the Nernst and activation relations were calculated according to the implemented PEMFC formulation. The hydrogen and air inlet pressures used by the electrochemical model were expressed in atmospheric units as

$$p_{H_2,nor} = \frac{p_{H_2,in}}{p_{ref}}, \qquad p_{air,nor} = \frac{p_{air,in}}{p_{ref}} \quad (32)$$

where $p_{H_2,in}$ and $p_{air,in}$ are the hydrogen and air inlet pressures [bar], respectively, while $p_{H_2,nor}$ and $p_{air,nor}$ are the corresponding normalized pressures [atm]. The reference atmospheric pressure is $p_{ref} = 1.01325$ bar, as reported in Table A3. The saturation pressure of water vapor was calculated as

$$p_{H_2O,sat} = 25.7 - 0.1615T_{stack} + 0.000255T_{stack}^2 \quad (33)$$

where $p_{H_2O,sat}$ is the saturation pressure of water vapor [atm]. The hydrogen partial pressure was then calculated as

$$p_{H_2} = p_{H_2,nor} \exp\left[-\frac{1.653I}{A_{PEM}T_{stack}^{1.334}}\right] - 0.5p_{H_2O,sat} \quad (34)$$

For air operation, the water-vapor mole fraction and the effective nitrogen diffusion term were calculated as

$$x_{H_2O} = \frac{p_{H_2O,sat}}{p_{air,nor}}, \qquad D_{N_2} = \frac{T_{stack}^{1.5}}{p_{air,nor}\left[83300 - 16700\left(p_{H_2O,sat}/p_{air,nor}\right)\right]} \quad (35)$$

where x_{H_2O} is the water-vapor mole fraction [−] and D_{N_2} is the effective nitrogen diffusion term used in the air-side formulation. To reduce the nitrogen mole-fraction expression, the auxiliary factor X_a was defined as

$$X_a = 0.79 - \frac{3.76S_{air}}{4.76S_{air} - 1} \quad (36)$$

where X_a is a dimensionless auxiliary factor. The nitrogen mole fraction was subsequently evaluated as

$$x_{N_2} = X_a\left(\frac{p_{air,nor} - p_{H_2O,sat}}{p_{air,nor}}\right)\left[\ln\left(0.21\left(4.76 - \frac{1}{S_{air}}\right)\right)\right]^{-1} \exp\left[\frac{5.315 \times 10^{-6}T_{stack}I}{A_{PEM}p_{air,nor}D_{N_2}}\right] \quad (37)$$

where x_{N_2} is the nitrogen mole fraction [−]. Finally, the oxygen partial pressure was calculated as

$$p_{O_2} = p_{air,nor}\left(1 - x_{H_2O} - x_{N_2}\right) \quad (38)$$

Water-vapor effects were represented through the saturation-pressure correction included in the reactant partial-pressure calculations; however, no independent dynamic humidification model was explicitly represented, and the evaporation fraction was set to $X_{EVAP} = 0$. These electrochemical boundary conditions were kept unchanged during the commercial-scale annual simulations; commercial scaling modified the number of cells, stacks, and modules rather than the underlying cell-level parameterization.

In contrast, the constant-efficiency representation (Case A) bypasses the electrochemical voltage–current response. The electrical power recovered from stored H_2 ($P_{PEMFC,const}$) is calculated using a fixed lower-heating-value efficiency ($\eta_{FC,const}$):

$$P_{PEMFC,const} = \min(P_{def}, P_{FC,installed}, \eta_{FC,const}\dot{n}_{H_2,out}LHV_{H_2,mol}) \quad (39)$$

Similarly, the required H_2 molar flow for a given PEMFC electrical demand ($P_{PEMFC,req}$) is directly mapped as

$$\dot{n}_{H_2,req} = \frac{P_{PEMFC,req}}{\eta_{FC,const}LHV_{H_2,mol}} \quad (40)$$

To highlight the fundamental differences between these two approaches, Table 6 summarizes how key parameters are computed in each model, referencing their respective formulations. The fixed physical constants and electrochemical parameters used in the PEMFC quasi-dynamic model are summarized in Table A3.

Table 6. Comparison between the constant-efficiency and quasi-dynamic PEMFC formulations.

Modeling Aspect	Constant-Efficiency PEMFC	Quasi-Dynamic PEMFC
Model basis	Fixed H_2-to-electricity conversion efficiency.	Generalized Amphlett–Mann electrochemical formulation [25–27].
Electrical output	Calculated using Equation (39).	Calculated from stack voltage and current using Equation (31).
Efficiency treatment	Fixed scalar value, $\eta_{FC,const}$.	Variable and dependent on the electrochemical operating point.
H_2 consumption	Direct proportional mapping using Equation (40).	Calculated from Faraday's law using Equation (31).
Voltage behavior	Not explicitly modeled.	Calculated using Equations (26) and (27).
Loss mechanisms	Not resolved.	Activation, ohmic, and concentration losses are included through Equations (28)–(30).
Main role	Baseline for system-level comparison.	Assessment of electrochemical and part-load effects.

For commercial-scale integration, the electrochemical formulation was preserved while the electrical architecture was adapted. The required PEMFC capacity ($P_{FC,req}$) was determined from the maximum electrical demand assigned to the H_2 subsystem. The number of commercial modules (N_{module}) and the total installed PEMFC capacity ($P_{FC,installed}$) are obtained as

$$N_{module} = \left\lceil \frac{P_{FC,req}}{P_{module}} \right\rceil, \qquad P_{FC,installed} = N_{module} P_{module} \tag{41}$$

where P_{module} is the electrical power delivered by a single commercial module. When more than one commercial configuration satisfies the required demand, the final configuration is selected by minimizing a size scoring penalty ($\mathcal{S}$):

$$\mathcal{S} = \frac{P_{FC,installed}}{P_{FC,req}} + w_c \min_j \left(\frac{|P_{module} - P_{class,j}|}{P_{class,j}} \right) \tag{42}$$

3.6. Hydrogen Storage and Auxiliary Compression Model

The H_2 storage subsystem was modeled as a pressurized gas tank coupled to the AEL, the PEMFC, and the auxiliary compressor. The formulation follows classical gas-storage thermodynamics based on the ideal-gas law and the van der Waals equation of state, as commonly used in H_2 energy-system simulations [61–63]. The hydrogen inventory in the tank (n_{H_2}) was updated at each simulation step as

$$n_{H_2}^{k+1} = n_{H_2}^{k} + \left(\dot{n}_{in}^{k} - \dot{n}_{out}^{k} - \dot{n}_{dump}^{k} \right) \Delta t \tag{43}$$

where $\dot{n}_{in}^{k}$ is the AEL molar inflow [mol s^{-1}], $\dot{n}_{out}^{k}$ is the PEMFC molar consumption [mol s^{-1}], $\dot{n}_{dump}^{k}$ is the vented H_2 flow [mol s^{-1}], and Δt is the simulation time step [s]. Normal volumetric H_2 flows were converted to molar flows using the auxiliary relation reported in Appendix B. The tank pressure was calculated using either the ideal-gas formulation (p_{tank}^{id}) or the van der Waals formulation (p_{tank}^{vdW}):

$$p_{tank}^{id} = \frac{n_{H_2} R T_{gas}}{V_{tank}}, \qquad p_{tank}^{vdW} = \frac{n_{H_2} R T_{gas}}{V_{tank} - n_{H_2} b} - a \left(\frac{n_{H_2}}{V_{tank}} \right)^2 \tag{44}$$

where T_{gas} is the gas temperature [K], V_{tank} is the tank volume [m^3], and a and b are the van der Waals constants. These constants were obtained from the critical properties of H_2, as reported in Appendix B. The tank state of charge (SOC_{tank}) and the vented H_2 flow used for overpressure protection ($\dot{n}_{dump}^{k}$) were represented as

$$SOC_{tank}^{k} = \frac{p_{tank}^{k}}{p_{max}}, \qquad \dot{n}_{dump}^{k} = \max\left(0, \frac{n_{H_2}^{k} - n_{H_2,max}}{\Delta t} \right) \tag{45}$$

where p^k_{tank} is the selected tank pressure formulation, p_{max} is the maximum allowable storage pressure (set to 350 bar in this study, while the dynamic minimum operating pressure $p_{tank,min}$ fluctuates between 6.5 and 6.9 bar depending on the case study), and $n_{H_2,max}$ is the maximum molar inventory compatible with p_{max}, T_{gas}, and V_{tank}. Tank pre-sizing and the storage dispatch logic are reported in Appendix B. The auxiliary compressor was represented using a single-equivalent-stage polytropic model. Compression was activated only when H_2 was injected into the tank and the final storage pressure exceeded the upstream pressure. The compressor molar flow ($\dot{n}_{\text{comp}}$) and the specific compression work (w_{comp}) were calculated as

$$\dot{n}_{\text{comp}} = \dot{V}_{\text{store,N}} \frac{p_{\text{ref}}}{RT_{\text{ref}}}, \qquad w_{\text{comp}} = \frac{\kappa}{\kappa - 1} RT_1 \left[\left(\frac{p_2}{p_1} \right)^{\frac{\kappa-1}{\kappa}} - 1 \right] \tag{46}$$

where $\dot{V}_{store,N}$ is the normal volumetric H_2 flow sent to storage [$\text{Nm}^3\ \text{s}^{-1}$], κ is the H_2 heat-capacity ratio, T_1 is the compressor inlet temperature [K], and p_1 and p_2 are the inlet and outlet pressures [bar]. The compressor electrical power (P_{comp}) and compressor energy consumption per time step (E^k_{comp}) were calculated as

$$P^k_{\text{comp}} = \frac{\dot{n}^k_{\text{comp}} w^k_{\text{comp}}}{\eta_{\text{comp}}}, \qquad E^k_{\text{comp}} = P^k_{\text{comp}} \Delta t \tag{47}$$

where η_{comp} is the compressor efficiency. The compressor is the only balance-of-plant parasitic load explicitly quantified in the present system-level energy balance. Accordingly, the auxiliary electrical demand considered in the simulations is defined as $P^k_{\text{aux}} = P^k_{\text{comp}}$. Other equipment-specific auxiliary loads associated with electrolyte circulation, cooling, gas separation, control systems, and water treatment are not modeled separately. In particular, the parasitic electricity demand associated with water desalination and deionization is excluded from the present simulation boundary. These additional BOP loads are excluded consistently from Cases A, A*, and B, and therefore do not introduce different auxiliary-load boundary conditions among the compared component-modeling approaches. Thus, compression reduces the net renewable surplus available for electrolysis and is included in the system-level energy balance. This treatment is consistent with H_2 storage studies where the AEL, compressor, tank, PEMFC, and power converters are modeled as coupled subsystems [63].

3.7. Renewable Energy Management and Annual Performance Assessment

Once the PV field, inverter, AEL, H_2 storage tank, compressor, and PEMFC are defined according to the procedures described in the previous sections, the complete PTP system is simulated chronologically over one year using the meteorological database and the corresponding electrical demand profile. At each simulation time step, PV generation is first assigned to the instantaneous electrical demand. The resulting surplus or deficit subsequently determines whether the H_2 pathway operates in charging or discharging mode. The same supervisory energy-management framework, minimum AEL operating-load criterion, storage constraints, and discharge logic are applied to all model configurations. Cases A and A* differ from Case B in the mathematical representation used to determine the AEL and PEMFC conversion behavior. Figure 2 summarizes the common supervisory framework and the component-level calculation sequences. The deterministic rule-based strategy was deliberately adopted to provide a common and transparent operating boundary for comparing the component-model formulations rather than to represent an optimal dispatch strategy. Alternative energy-management strategies could modify the distribution of AEL and PEMFC operating points and, consequently, the absolute annual performance and the magnitude of the differences between the model configurations. Therefore, the com-

parative results reported in this study should be interpreted as conditional on the common supervisory strategy adopted here.

The instantaneous renewable power balance is calculated as

$$P^k_{\text{bal}} = P^k_{\text{PV,AC}} - P^k_{\text{load}} \tag{48}$$

where $P^k_{\text{PV,AC}}$ is the AC power delivered by the PV system [W], P^k_{load} is the instantaneous electrical demand [W], and k denotes the simulation time step. The corresponding surplus and deficit powers are obtained as

$$P^k_{\text{sur}} = \max\left(0, P^k_{\text{bal}}\right), \qquad P^k_{\text{def}} = \max\left(0, -P^k_{\text{bal}}\right) \tag{49}$$

Positive values of P^k_{bal} identify intervals in which renewable electricity is available for the H_2 production pathway, whereas negative values identify intervals in which stored H_2 can be used for electricity recovery according to the discharge strategy. Charging and discharging are treated as mutually exclusive operating modes. During charging intervals, PEMFC generation is disabled; during discharge intervals, the storage model does not simultaneously admit newly produced H_2. The tank inventory obtained at the end of each time step is transferred to the subsequent step, thereby maintaining the chronological coupling among hydrogen production, storage, and reconversion.

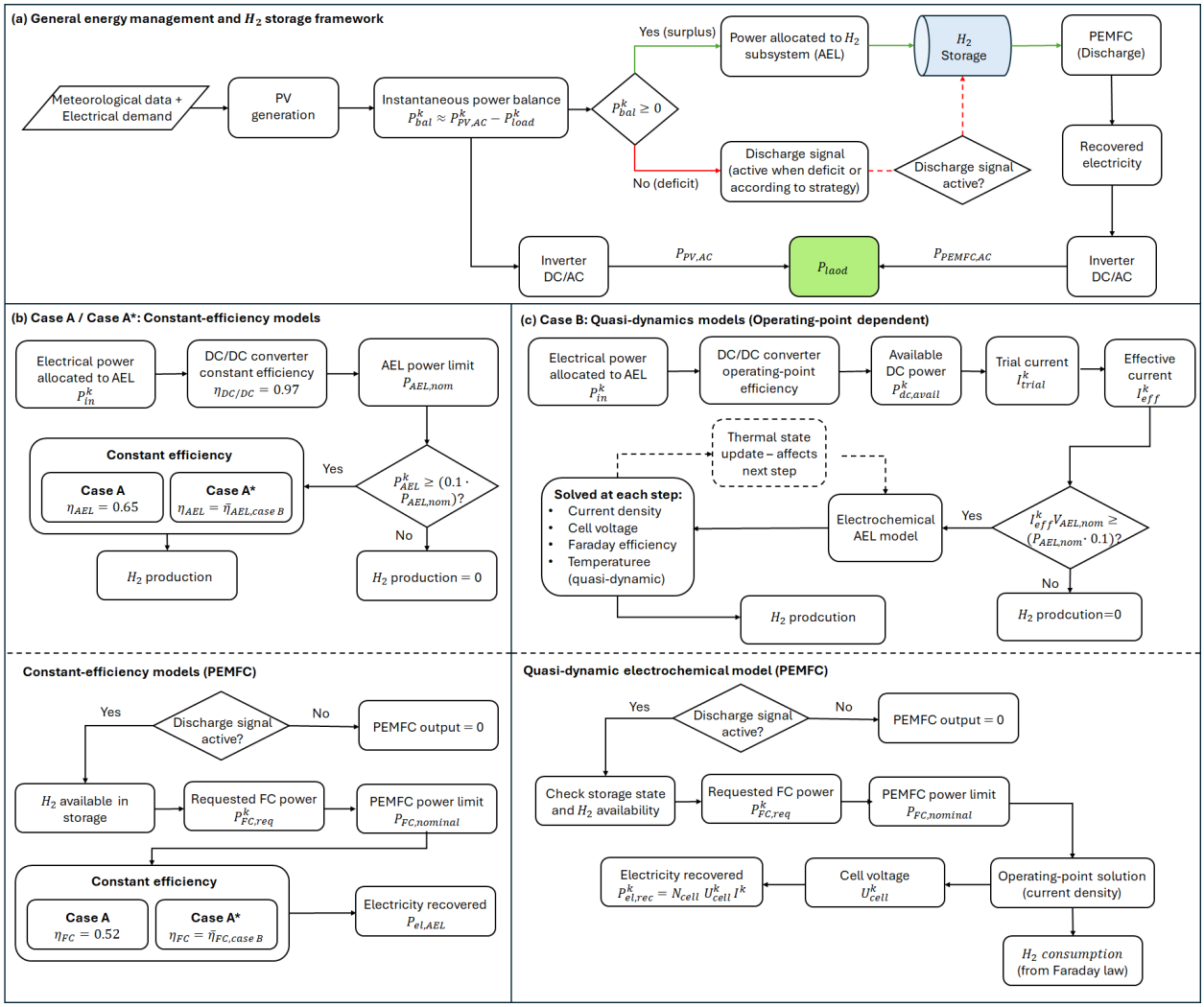


Figure 2. Energy-management framework and component-model calculation sequences for the PTP system: (**a**) common supervisory framework for renewable-surplus storage and deficit-period electricity recovery; (**b**) constant-efficiency AEL and PEMFC representations used in Cases A and A*; and (**c**) operating-point-dependent quasi-dynamic AEL and PEMFC representations used in Case B.

As shown in Figure 2a, when renewable surplus is available, electrical power is allocated to the H_2 subsystem according to the storage-sizing configuration under evaluation. Before H_2 production is enabled, the AEL must satisfy a minimum operating-load condition. A lower operating limit corresponding to 10% of the nominal AEL power is adopted for all configurations:

$$P^{k}_{\mathrm{AEL}} \geq P_{\mathrm{AEL,min}} = 0.10 P_{\mathrm{AEL,nom}} \tag{50}$$

where $P_{\mathrm{AEL,nom}}$ is the nominal electrical power of the selected commercial electrolyzer [W]. Minimum-load limitations are particularly relevant for alkaline electrolysis because hydrogen crossover becomes increasingly important relative to the total gas production at low current densities, increasing the H_2 concentration in the O_2 stream and constraining safe operation. Minimum operating loads between approximately 10% and 40% are reported for alkaline electrolyzers, depending on operating pressure, temperature, diaphragm characteristics, and electrolyte configuration [64]. Low-load operation under variable renewable supply also introduces relevant limitations associated with efficiency, gas purity, and operational safety [65]. Accordingly, 10% is selected as the lower operating boundary in the present analysis, representing the lower end of the reported operating range while preserving the flexibility required for coupling with variable PV generation. If the available AEL power does not satisfy Equation (50), H_2 production is set to zero for that time step.

The H_2 generated during charging is subsequently transferred to the storage subsystem subject to the tank capacity and pressure constraints described in Section 3.6. The compressor electrical demand is calculated only for the hydrogen flow effectively admitted into the storage tank. During deficit periods, the discharge signal enables H_2 withdrawal when the corresponding dispatch condition is satisfied and the storage inventory and pressure remain above their prescribed minimum values. The requested PEMFC power is subsequently constrained by the nominal installed capacity. This supervisory logic is common to Cases A, A*, and B; the principal distinction among the configurations lies in how the conversion processes within the AEL and PEMFC are represented.

For Cases A and A*, shown in Figure 2b, the DC/DC converter is represented using the constant efficiency $\eta_{\mathrm{DC/DC}} = 0.97$. The electrical power supplied to the AEL is first constrained by the nominal capacity of the selected commercial unit and by the minimum-load criterion defined in Equation (50). Once this condition is satisfied, H_2 production is obtained using the constant-efficiency formulation described in Section 3.4. The conversion efficiency is therefore prescribed independently of instantaneous current density, cell voltage, and electrolyzer thermal state. Case A uses a fixed AEL efficiency of $\eta_{\mathrm{AEL}} = 0.65$ on an LHV basis, representing a literature-based nominal reference value rather than an annual or seasonal mean efficiency. This value is consistent with the nominal stack efficiency of approximately 65% reported for commercial alkaline electrolysis systems [56]. Case A* retains the same algebraic formulation and supervisory logic but uses the annual energy-equivalent AEL efficiency derived from Case B.

The Case B AEL follows the operating-point-dependent sequence illustrated in Figure 2c. The DC/DC conversion efficiency is first evaluated at the corresponding operating condition, after which the available DC power is used to estimate a trial stack current. The electrochemical model then determines the associated stack voltage and the effective current consistent with the electrical and electrochemical operating limits. The resulting AEL power is evaluated against the same 10% minimum-load condition applied to Cases A and A*. If this condition is satisfied, current density, cell voltage, Faraday efficiency, H_2 production, and electrolyzer temperature are calculated using the electrochemical and thermal relations introduced in Section 3.4.

The resulting thermal state is transferred to the subsequent simulation step, preserving the slower thermal response within the chronological calculation. The quasi-dynamic

AEL formulation therefore accounts for thermal inertia through the propagated lumped thermal state [29,30]. Reviews of renewable-driven electrolysis distinguish the fast electrical response from slower variables such as temperature and pressure, which become relevant during variable operation [34]. However, the present model does not impose an additional empirical start-up energy penalty or minimum warm-up duration. Such plant-level start-up and shut-down sequences depend on equipment-specific thermal, pressure, and auxiliary-system conditions and are outside the scope of the present system-level formulation.

Consequently, the minimum-load threshold determines whether H_2 production is permitted in all configurations, whereas the conversion behavior above this threshold differs fundamentally. In Cases A and A*, H_2 production remains proportional to the processed electrical power because η_{AEL} is prescribed. In Case B, H_2 production is determined from the electrochemical operating point: Faraday efficiency varies with current density, while the cell voltage depends on the electrical load and thermal state. Thus, the quasi-dynamic formulation can predict different H_2 production rates from the constant-efficiency formulation even when both configurations satisfy the same minimum-load criterion. The 10% threshold therefore determines whether AEL operation is enabled, whereas the component model determines the conversion performance once operation begins.

A similar distinction applies to the electricity-recovery stage. In Cases A and A*, the PEMFC is activated when the discharge signal is enabled and sufficient H_2 is available in storage. The requested electrical power is limited by the installed PEMFC capacity, and the corresponding H_2 consumption and electrical output are determined using the constant-efficiency formulation presented in Section 3.5. Case A uses a fixed PEMFC electrical efficiency of $\eta_{FC} = 0.52$, representing a literature-based nominal-load reference value rather than an annual or seasonal mean efficiency. A comparable fixed efficiency of 52% is adopted for the PEMFC in an integrated off-grid renewable-hydrogen system reported by Ju et al. [57]. Case A* uses the annual energy-equivalent PEMFC efficiency obtained from Case B while retaining the simplified constant-efficiency formulation.

For Case B, the discharge request and storage-availability constraints are applied before solving the quasi-dynamic PEMFC model. The requested power is constrained by the nominal PEMFC capacity, after which the admissible operating point is determined using the polarization-based formulation described in Section 3.5. The resulting current density and cell voltage determine the recoverable electrical power, while H_2 consumption follows the corresponding electrochemical reaction rate. Electricity recovery therefore depends on the instantaneous PEMFC operating point rather than on a prescribed conversion efficiency. If the storage or component operating constraints cannot satisfy the requested condition, the PEMFC electrical output is set to zero.

Case A* is introduced as a controlled sensitivity of the constant-efficiency formulation to distinguish the influence of the prescribed constant-efficiency values from the effect of suppressing operating-point dependence. The annual energy-equivalent AEL and PEMFC efficiencies are obtained from the corresponding Case B annual energy balances, as defined in Equations (7) and (8), and are subsequently used as fixed values in Case A*. The comparison between Case A and Case A* therefore quantifies the influence of the selected fixed efficiency values, while the comparison between Case A* and Case B assesses the differences that remain when annual energy-equivalent efficiencies are retained within a constant-efficiency formulation instead of resolving the component operating point at each simulation step.

The chronological simulation provides the annual energy quantities required for the system-level assessment. The annual direct PV electricity supplied to the demand and the annual electrical demand are calculated as

$$E_{\mathrm{PV,direct}} = \sum_{k=1}^{N} \min\left(P^{k}_{\mathrm{PV,AC}}, P^{k}_{\mathrm{load}}\right)\Delta t, \qquad E_{\mathrm{load}} = \sum_{k=1}^{N} P^{k}_{\mathrm{load}}\Delta t \tag{51}$$

The annual electricity consumed by the AEL, the auxiliary electrical consumption, and the electricity recovered by the PEMFC are calculated as

$$E_{\mathrm{AEL}} = \sum_{k=1}^{N} P^{k}_{\mathrm{AEL}}\Delta t, \qquad E_{\mathrm{aux}} = \sum_{k=1}^{N} P^{k}_{\mathrm{aux}}\Delta t, \qquad E_{\mathrm{PEMFC}} = \sum_{k=1}^{N} P^{k}_{\mathrm{PEMFC}}\Delta t \tag{52}$$

where P^{k}_{aux} [W] represents the auxiliary electrical consumption included within the system boundary, principally the H_2 compression demand considered in the storage model. The total annual renewable electricity supplied to the demand through direct PV generation and H_2 reconversion is then calculated as

$$E_{\mathrm{REN,PTP}} = E_{\mathrm{PV,direct}} + E_{\mathrm{PEMFC}} \tag{53}$$

and the corresponding annual renewable fraction is

$$SF_{\mathrm{PTP}} = \frac{E_{\mathrm{REN,PTP}}}{E_{\mathrm{load}}} \tag{54}$$

The modeled PV–H_2 subsystem is not intended to represent the complete Santa Cruz–Baltra generation portfolio or an autonomous electricity system. The annual indicator SF_{PTP} quantifies only the fraction of electrical demand supplied directly by PV generation and by electricity recovered through the H_2 pathway. Whenever $SF_{\mathrm{PTP}} < 1$, the residual demand, $E_{\mathrm{load}} - E_{\mathrm{REN,PTP}}$, must be supplied by the background island power system and lies outside the present modeling boundary. Conventional-generation dispatch, fuel consumption, electricity cost, and emissions associated with this residual supply are therefore not included in the present component-modeling comparison. Thus, the annual PTP efficiency is defined as

$$\eta_{\mathrm{PTP}} = \frac{E_{\mathrm{PEMFC}}}{E_{\mathrm{AEL}} + E_{\mathrm{aux}}} \tag{55}$$

which represents the annual electricity-to-H_2-to-electricity performance of the storage pathway rather than the efficiency associated with direct PV supply to the electrical demand. Finally, the chronological calculation is repeated across the evaluated PV-field and H_2-storage design space. The design objective is to maximize the fraction of the annual electrical demand supplied by the renewable PTP system within the evaluated parametric space. Accordingly, the PV field area and the available H_2 storage capacity are varied parametrically to quantify their influence on renewable electricity coverage, rather than imposing a predefined condition of complete electrical autonomy or zero loss of power supply probability. For each H_2 storage configuration, the PV capacity producing the maximum renewable fraction is identified as

$$SF_{\mathrm{PTP,max}} = \max_{i}\left(SF_{\mathrm{PTP},i}\right), \qquad i^{*} = \arg\max_{i}\left(SF_{\mathrm{PTP},i}\right), \qquad P_{\mathrm{PV,opt}} = P_{\mathrm{PV},i^{*}} \tag{56}$$

This procedure provides a common design objective for Cases A, A*, and B, while allowing the resulting renewable fraction and subsystem sizing to vary according to the component-level conversion formulation.

4. Results

The results are presented in three stages. First, the generated P_{24h} and the resulting 6 min $P_{i,d}$ profile are examined to verify the temporal demand input used in the PTP simulations. Second, the AEL and PEMFC implementations are validated before applying them to commercial-scale operation. Third, the annual energy results are evaluated for Case A and Case B, with emphasis on η_{PTP}, E_{PEMFC}, and the relative differences $RD_{\eta_{PTP}}$ and $RD_{E_{PEMFC}}$.

4.1. Demand Profile Generation

The resulting P_{24h} and $P_{i,d}$ are shown in Figure 3. Figure 3a shows the normalized 24 h demand shape used as the intraday allocation input, while Figure 3b shows the generated 6 min temporal $P_{i,d}$ profile for the annual simulation. The profile preserves the imposed daily shape, the monthly energy allocation, the temperature-dependent seasonal modulation, and the target peak-demand constraint introduced in Section 3.1. From the prescribed annual electricity consumption of 41.99 GWh and the target peak demand of 7.51 MW, the resulting annual average load is approximately 4.79 MW, corresponding to an annual load factor of approximately 0.638. A coincidence factor was not calculated because the available information does not include disaggregated customer- or feeder-level noncoincident peak demands. Likewise, no measured subhourly Santa Cruz–Baltra demand series was publicly available for direct validation of the generated daily curves. Therefore, the profile is assessed against the available annual-energy, monthly-allocation, intraday-shape, and peak-demand constraints and is used as a common temporal boundary condition for comparing Cases A and B rather than as a validated reconstruction of measured feeder-level operation.

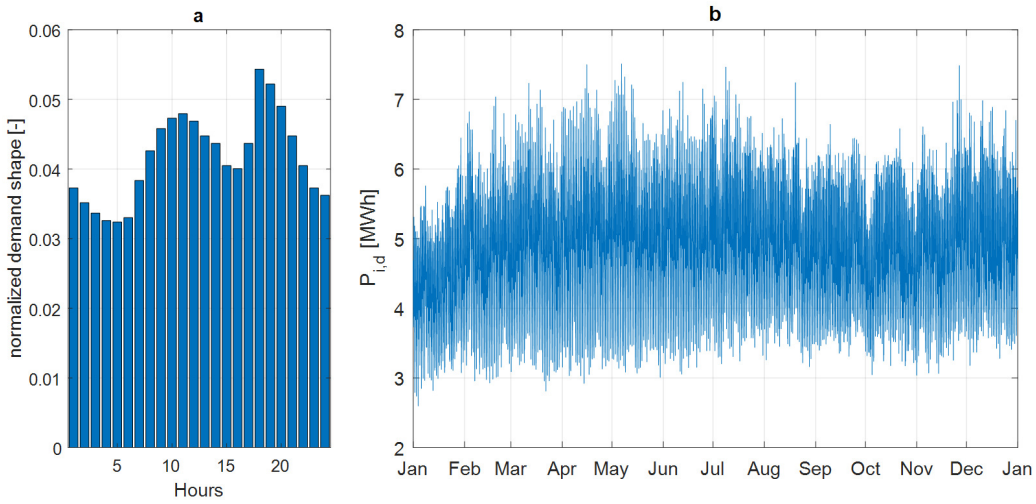


Figure 3. Santa Cruz–Baltra demand input: (**a**) normalized P_{24h} and (**b**) generated 6 min $P_{i,d}$ profile.

4.2. AEL Validation

The AEL implementation was first verified by reproducing the reference voltage–current curves of the quasi-dynamic alkaline-electrolyzer formulation at 40, 60, and 80 °C, as shown in Figure 4a [30]. Figure 4b–d present the corresponding regressions obtained at 40, 60, and 80 °C, respectively. The resulting $R^2 = 0.99904$ confirms that the MATLAB Version 24.2 (R2024b) implementation reproduces the reference voltage–current behavior with negligible deviation.

After verifying the implementation, the quasi-dynamic AEL model was externally validated using the experimental polarization curves reported by Sánchez et al. for a 15 kW alkaline electrolyzer [66]. The model parameters summarized in Table A2 were

used as the initial literature-based parameter set. However, because the Sánchez et al. system corresponds to a specific experimental stack, the validation used the stack geometry and operating conditions reported in that study. The empirical voltage coefficients and effective thermal parameters were then calibrated while preserving the original quasi-dynamic model equations. Therefore, the calibration should be interpreted as a stack-specific parameterization of the quasi-dynamic AEL model for the Sánchez et al. experimental system. The validation-specific inputs and calibrated parameters are summarized in Table 7.

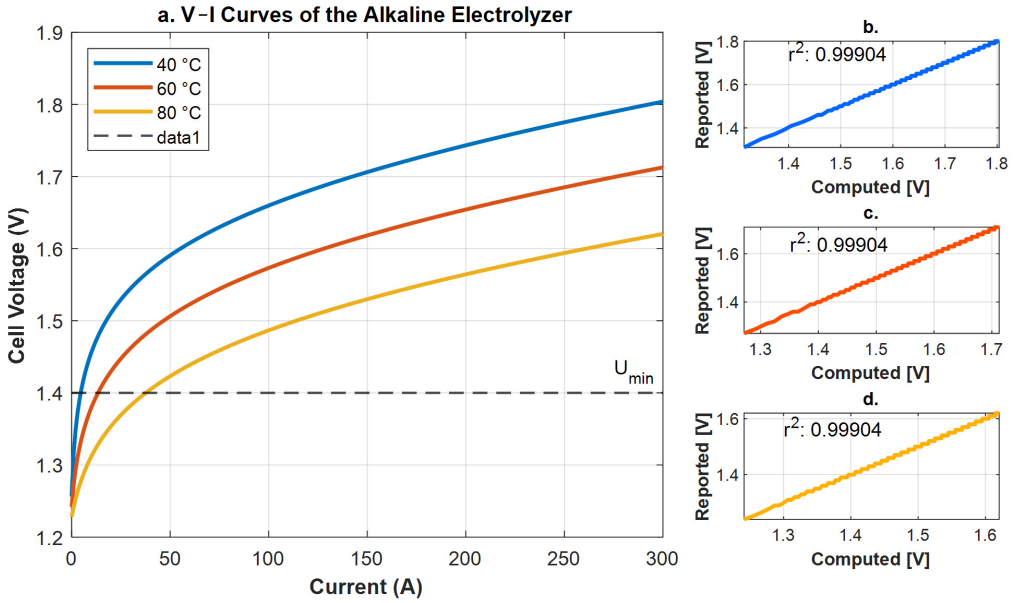


Figure 4. Verification of the quasi-dynamic AEL model implementation: (**a**) voltage–current curves at 40, 60, and 80 °C; (**b**) regression at 40 °C; (**c**) regression at 60 °C; (**d**) regression at 80 °C.

Table 7. Validation-specific inputs and calibrated parameters used to reproduce the Sánchez et al. experimental AEL polarization curves.

Parameter	Value	Source or Definition
Number of cells, N_{cells}	12	[66]
Active cell area, A_e	1000 cm^2	[66]
Operating temperature	55, 65, and 75 °C	[66]
Operating pressure	5 and 7 bar	[66]
r_1	5.840449×10^{-5}	Calibrated in this work
r_2	-1.296316×10^{-7}	Calibrated in this work
s_1	3.018500×10^{-1}	Calibrated in this work
t_1	-2.288456×10^{-2}	Calibrated in this work
t_2	3.100032	Calibrated in this work
t_3	1.331780×10^{1}	Calibrated in this work
h_1	1.000375×10^{-1}	Calibrated in this work
h_2	1.018314×10^{-1}	Calibrated in this work
R_T	2.346866×10^{-1} K W^{-1}	Calibrated in this work
τ_T	265.4395 h	Calibrated in this work
$T_{cw,in}$	4.673899 °C	Calibrated in this work
$\dot{V}_{cw}$	41.45471 Nm^3 h^{-1}	Calibrated in this work

Figure 5 compares the calibrated quasi-dynamic AEL model with the experimental polarization data reported by Sánchez et al. Figure 5a shows the effect of temperature at 7 bar, while Figure 5b shows the effect of pressure at 75 °C. The model reproduces the mono-

tonic increase of stack voltage with AEL current density, J_{AEL}, and captures the expected reduction in voltage as the operating temperature increases. The simulated curves were extended from near-zero current density to assess the initial change in slope characteristic of alkaline-electrolyzer polarization curves. The relative difference factor, RD, was obtained by comparing the stack-voltage values predicted by the quasi-dynamic model described in the methodology with the digitized experimental values reported by Sánchez et al. [66] RDF values were evaluated only at the digitized experimental points, whereas the low-current region was included only to visualize the modeled polarization behavior near open-circuit operation.

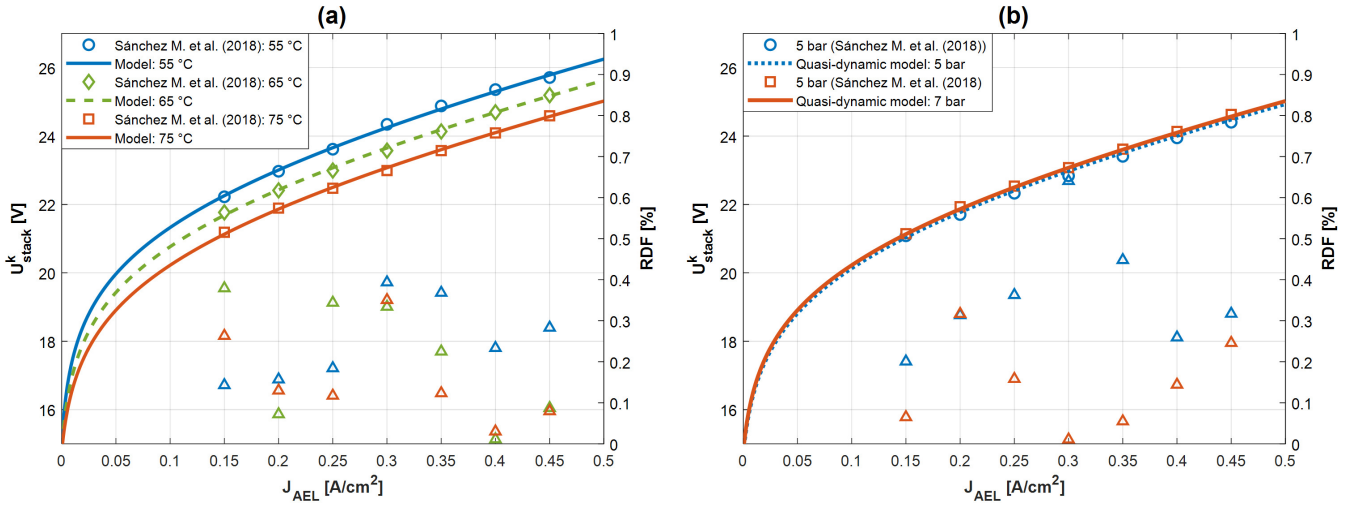


Figure 5. Validation of the calibrated quasi-dynamic AEL model using the Sánchez et al. [66] experimental polarization curves: (**a**) temperature effect at 7 bar; (**b**) pressure effect at 75 °C. Open markers denote experimental data, lines denote model predictions, and colored triangles denote RD values shown on the right axis.

The comparison shows that the calibrated quasi-dynamic AEL model provides a suitable representation of the experimental polarization behavior in the evaluated current-density range. In Figure 5a, the voltage decreases as temperature increases, which is consistent with the expected reduction of reversible voltage and activation losses at higher operating temperature. In Figure 5b, the model also follows the voltage level observed at different pressures, although the pressure effect is less pronounced than the temperature effect. The RDF values remain low across the digitized points, confirming that the calibrated parameter set can reproduce the measured stack-voltage response of the Sánchez et al. system. This result supports the use of the quasi-dynamic AEL formulation in the subsequent PV–AEL simulations, where hydrogen production and efficiency depend on the instantaneous operating current density and thermal state.

4.3. PEMFC Validation

The generalized Amphlett–Mann PEMFC implementation was assessed using the experimental polarization data reported by Toharias et al. [60]. The digitized current-density data and the active membrane area (A_{PEM}) were used as model inputs, while the cell voltage (V_{cell}) was compared against the experimental values. A limited calibration step was performed by varying the effective cell pressure (p_{cell}) and PEM thickness (t_{PEM}) within prescribed ranges and selecting the parameter pair that minimized the root mean square error (RMSE). The governing electrochemical equations were not modified during this calibration.

The validation results are shown in Figure 6. Figure 6a presents the RMSE distribution used to identify the best-fit parameter pair, while Figure 6b compares the experimental and simulated polarization curves obtained with the calibrated configuration. The minimum RMSE was 0.0123 V, indicating good agreement between the implemented PEMFC model and the digitized experimental data. The model reproduces the activation and ohmic regions with good agreement, while small deviations appear at high current density, where concentration effects become more relevant. These results support the use of the calibrated PEMFC implementation for the commercial-scale PTP simulations.

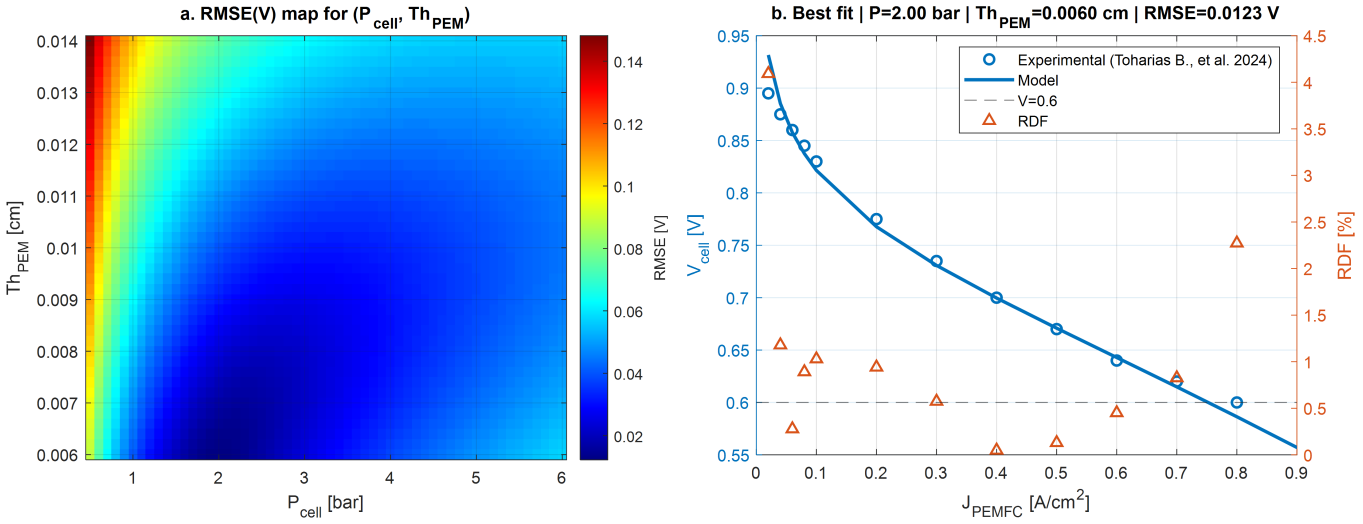


Figure 6. PEMFC validation: (**a**) RMSE distribution and (**b**) experimental and simulated polarization curves [60].

4.4. Energy Performance of Case A and Case B

After validating the AEL and PEMFC models, the annual PTP simulations were performed for Case A and Case B using the same $P_{i,d}$, PV generation profile, H_2 storage parameters, compressor model, component capacities, and supervisory control logic. Case A uses constant efficiencies for both conversion stages, whereas Case B uses the quasi-dynamic AEL and PEMFC models. The comparison in this subsection focuses first on the spatial response of η_{PTP} and *SF* as a function of PV field area and H_2 storage hours. Figures 7 and 8 shows a representative daily operating window for Case A and Case B. Both cases are evaluated under the same PV generation and demand conditions, but the resulting H_2 production, storage evolution, and PEMFC electricity recovery differ because of the component-modeling approach.

In Case A, the constant-efficiency representation produces a more direct proportional relation between PV surplus, AEL operation, H_2 production, and PEMFC output. In Case B, the quasi-dynamic AEL and PEMFC models modify this response, producing a different H_2 generation profile and a discharge pattern concentrated during nighttime deficit periods. This behavior illustrates, at the time-series level, why the two cases lead to different annual η_{PTP}, *SF*, and E_{PEMFC} response surfaces. Figure 9 compares the resulting η_{PTP} maps for both cases. The horizontal axis represents the PV field area, while the vertical axis represents the H_2 storage hours available to supply demand during periods without solar generation. The color map represents η_{PTP}, the solid white contours indicate selected η_{PTP} levels, and the dashed black contours represent *SF*.

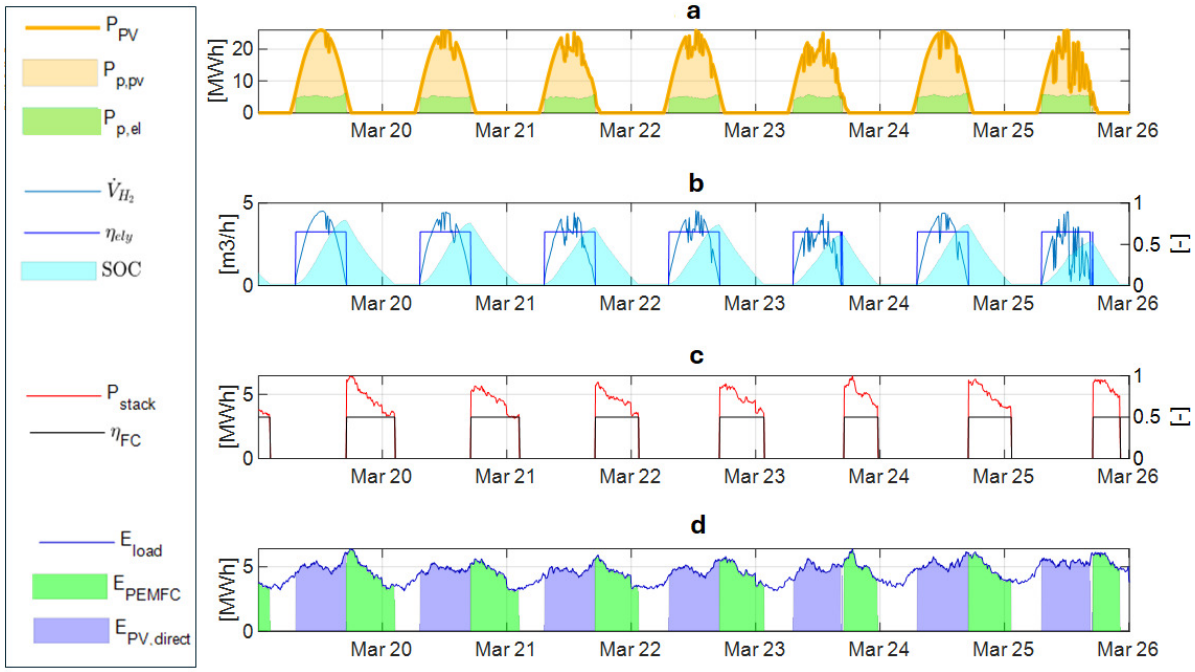


Figure 7. Case A with constant efficiencies: Representative daily operation of the PV–AEL–H_2–PEMFC system: (**a**) PV generation and electricity allocation to direct load supply and the electrolyzer; (**b**) H_2 production, storage state of charge, and electrolyzer efficiency; (**c**) PEMFC electricity generation and efficiency; and (**d**) electrical demand and contributions from direct PV supply and PEMFC generation.

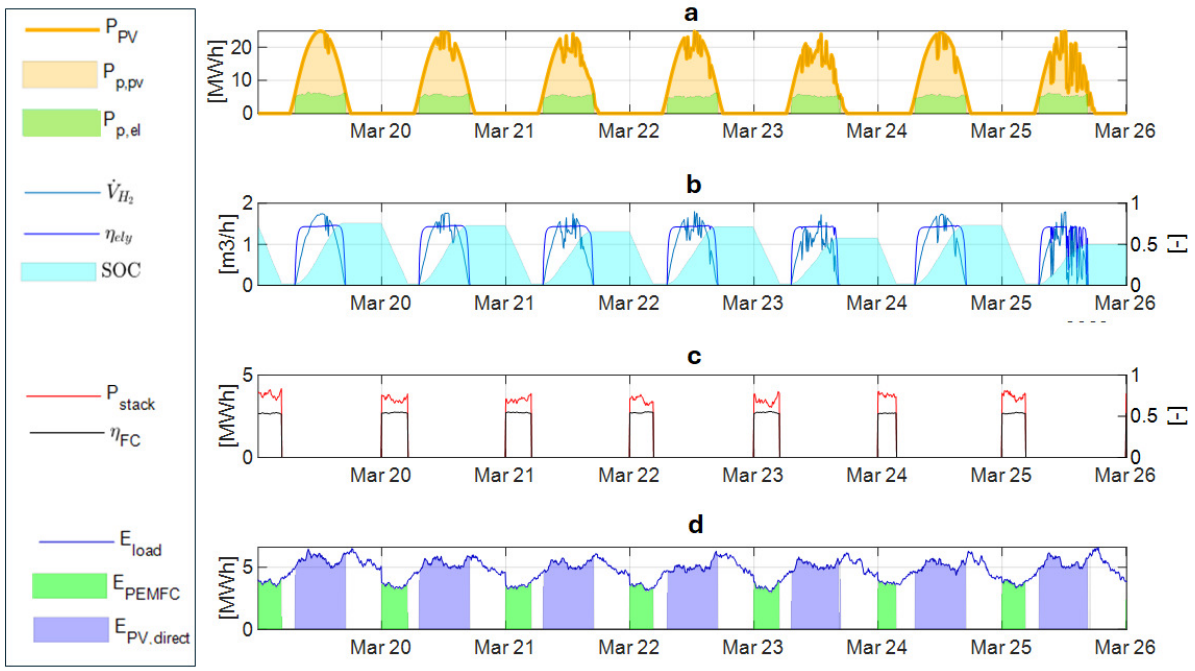


Figure 8. Case B with quasi-dynamic AEL and PEMFC models: Representative daily operation of the PV–AEL–H_2–PEMFC system: (**a**) PV generation and electricity allocation to direct load supply and the electrolyzer; (**b**) H_2 production, storage state of charge, and electrolyzer efficiency; (**c**) PEMFC electricity generation and efficiency; and (**d**) electrical demand and contributions from direct PV supply and PEMFC generation.

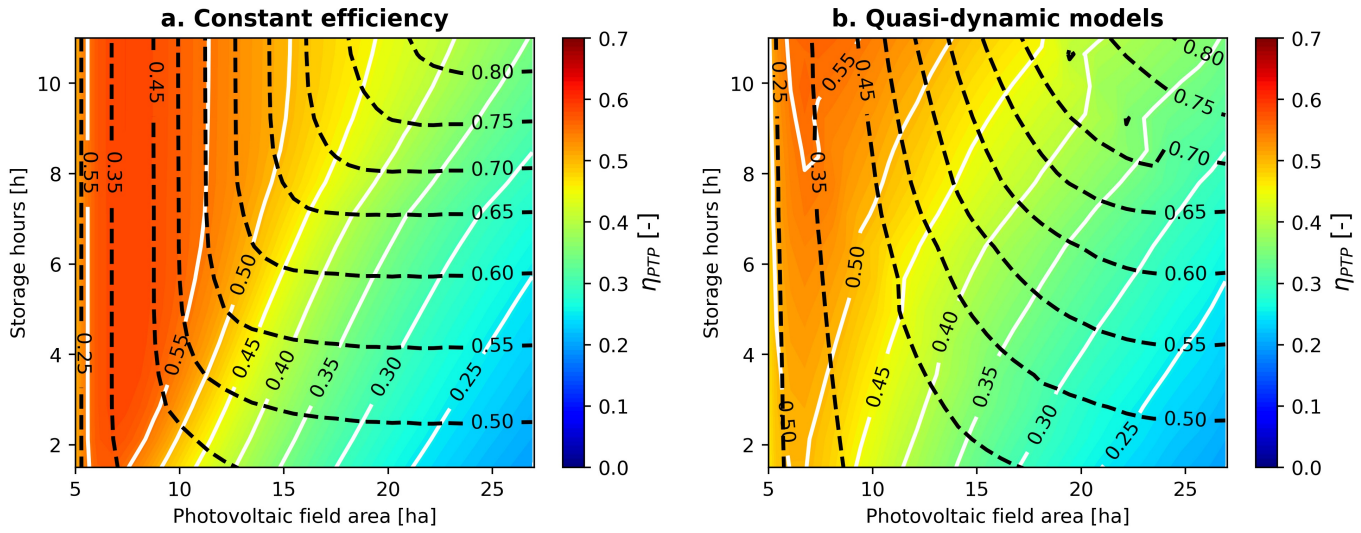


Figure 9. Comparison of η_{PTP} and *SF* for the two model configurations: (**a**) Case A with constant AEL and PEMFC efficiencies and (**b**) Case B with quasi-dynamic AEL and PEMFC models.

For Case A, shown in Figure 9a, η_{PTP} decreases progressively as the PV field area increases. The highest η_{PTP} values are concentrated at the lower PV-area range, while larger PV fields lead to lower values across most storage-hour conditions. The white contours show a smooth and nearly monotonic transition from high to low η_{PTP} as the PV field area increases. In this case, the *SF* contours show a comparatively regular behavior. After η_{PTP} approaches approximately 0.45, the dashed *SF* contours tend to maintain a more linear pattern with respect to the PV field area, indicating a more uniform relation between PV sizing, storage duration, and renewable coverage under the constant-efficiency assumption.

For Case B, shown in Figure 9b, the η_{PTP} field also decreases with increasing the PV field area, but the contour structure is less regular than in Case A. The white η_{PTP} contours present stronger curvature and local changes in slope, particularly at intermediate PV field areas and higher storage-hour conditions. This indicates that the quasi-dynamic representation modifies the relationship between PV field area, storage duration, and the recovered electricity pathway. The dashed *SF* contours also show a different pattern from Case A. Instead of maintaining the same nearly linear behavior after the intermediate η_{PTP} range, *SF* tends to decrease as the PV field area continues to increase in several regions of the map. This change is more visible at larger PV areas, where the quasi-dynamic conversion behavior alters the combined response of η_{PTP} and *SF*.

Overall, the comparison shows that both cases predict higher η_{PTP} at smaller PV field areas and lower η_{PTP} at larger PV field areas. However, the transition pattern differs between the two cases. Case A produces smoother and more regular η_{PTP} and *SF* contours, whereas Case B produces a more variable contour structure. These results indicate that the quasi-dynamic AEL and PEMFC models affect not only the magnitude of η_{PTP}, but also the trend between η_{PTP}, *SF*, PV field area, and H_2 storage hours.

Figure 10 shows the relative difference between Case A and Case B. Figure 10a presents $RD_{\eta_{PTP}}$, whereas Figure 10b presents $RD_{E_{PEMFC}}$. In both maps, the horizontal axis represents the PV field area and the vertical axis represents the H_2 storage hours. The color map and the white contour lines represent the corresponding relative difference.

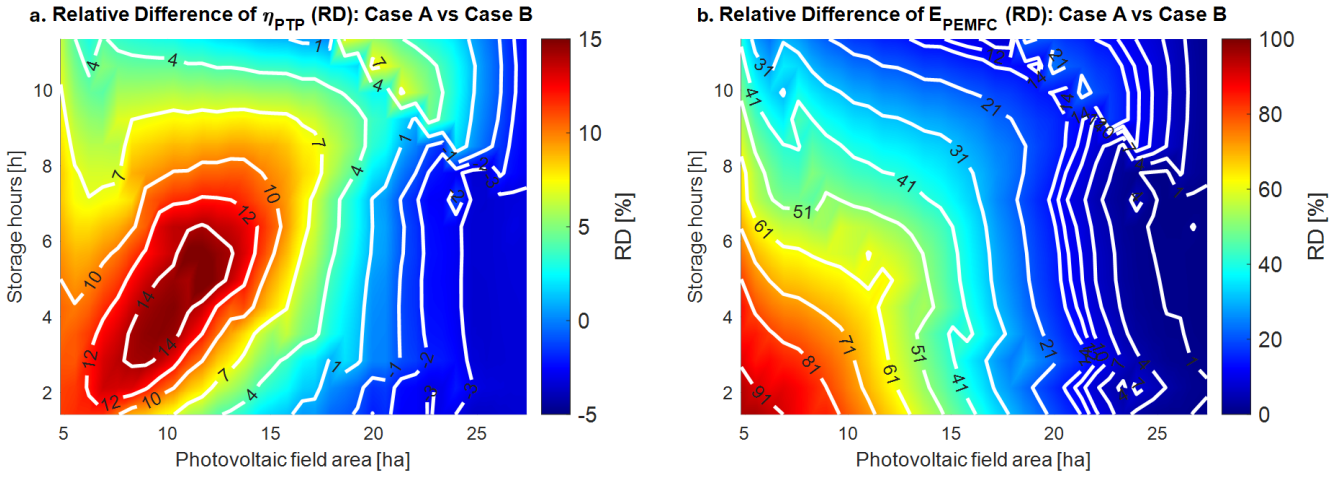


Figure 10. Relative difference between Case A and Case B: (**a**) $RD_{\eta_{PTP}}$ and (**b**) $RD_{E_{PEMFC}}$.

For $RD_{\eta_{PTP}}$, Figure 10a shows that the constant-efficiency case predicts higher η_{PTP} than the quasi-dynamic case over a wide region of the design space. The maximum increase is approximately 14%, concentrated around a PV field area close to 10 ha and a storage duration of approximately 4 h. Positive values dominate the low-to-intermediate PV area range, while the relative difference decreases as the PV field area increases. At larger PV field areas, the map shows regions with values close to zero and negative values, indicating that the quasi-dynamic case can locally predict equal or higher η_{PTP} than the constant-efficiency case.

For $RD_{E_{PEMFC}}$, Figure 10b shows substantially larger differences than those observed for η_{PTP}. The maximum increase reaches approximately 91%, mainly within the low-storage and low-PV-area region. This behavior is associated with the high sensitivity of PEMFC electricity recovery to H_2 availability under constrained conditions. In this region, small differences in AEL H_2 production, tank state of charge, and PEMFC operating efficiency can determine whether the fuel cell is dispatched during deficit periods. The constant-efficiency case behaves as a proportional conversion pathway, whereas the quasi-dynamic case introduces current-density, thermal, and polarization effects that modify H_2 production and consumption at each operating point. This is relevant for subsequent techno-economic indicators, since overestimating H_2 production or recovered PEMFC electricity can change the apparent utilization of the system and the useful-energy denominator used in LCOE calculations. As the PV field area increases, more surplus energy becomes available for electrolysis, the H_2 inventory constraint is relaxed, and $RD_{E_{PEMFC}}$ decreases progressively.

Overall, the relative-difference maps show that the constant-efficiency assumption affects E_{PEMFC} more strongly than η_{PTP}. While $RD_{\eta_{PTP}}$ remains mostly within a range of approximately −5 to 15%, $RD_{E_{PEMFC}}$ extends up to approximately 91%. Therefore, the effect of the modeling assumption is more pronounced in the annual electricity recovered by the PEMFC than in the global PTP efficiency.

4.5. Sensitivity of the Constant-Efficiency Baseline

To assess the sensitivity of the results to the constant efficiency values adopted in Case A, the additional Case A* configuration defined in Section 3.3 is evaluated. Case A* retains the constant-efficiency formulation of Case A but uses the annual energy-equivalent AEL and PEMFC efficiencies obtained from Case B. The relative differences between Case A* and Case B are shown in Figure 11, where Figure 11a presents the global PTP efficiency and Figure 11b presents the annual electricity recovered by the PEMFC.

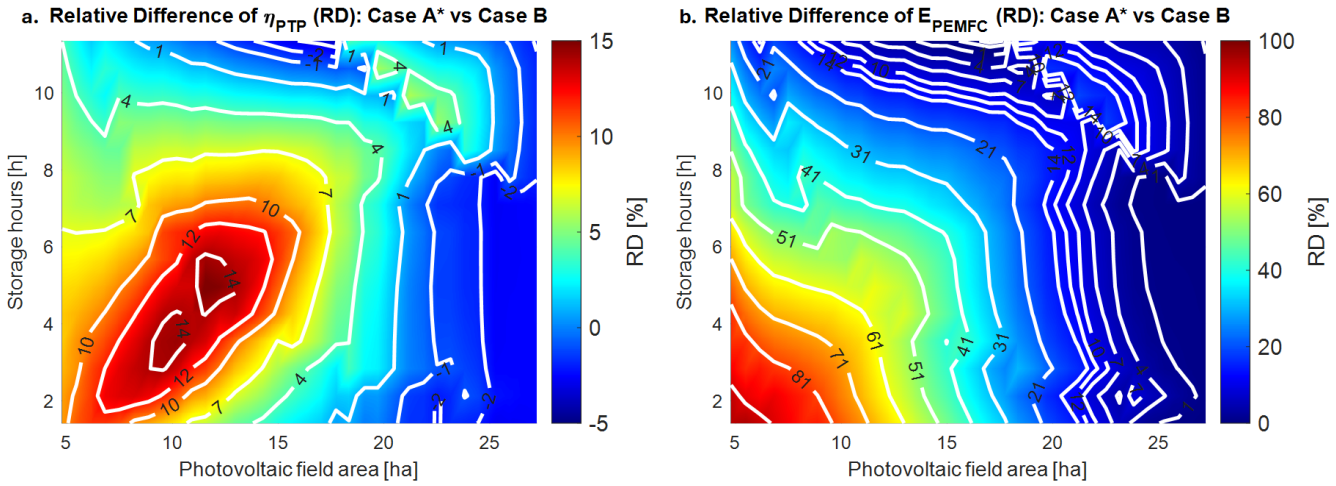


Figure 11. Relative difference between Case A* and Case B as a function of photovoltaic field area and H_2 storage duration: (**a**) global PTP efficiency, $RD_{\eta_{PTP}}$, and (**b**) annual electricity recovered by the PEMFC, $RD_{E_{PEMFC}}$.

As shown in Figure 11a, $RD_{\eta_{PTP}}$ varies approximately from −5% to 15% across the evaluated design space. The highest positive differences are concentrated at low-to-intermediate PV field areas and intermediate H_2 storage durations, while values close to zero and negative differences occur mainly at larger PV field areas. Figure 11b shows substantially larger differences for E_{PEMFC}, reaching values above 80% at low PV field areas and short storage durations and decreasing progressively as the PV field area increases. The relative differences between Case A* and the original Case A are shown in Figure 12, where Figure 12a corresponds to $RD_{\eta_{PTP}}$ and Figure 12b corresponds to $RD_{E_{PEMFC}}$.

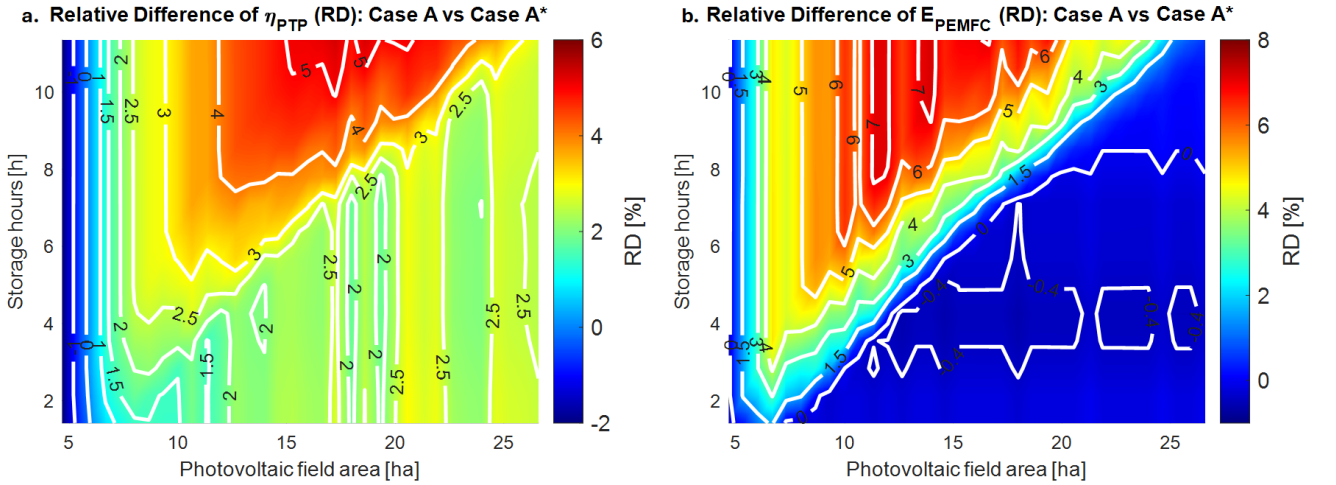


Figure 12. Relative difference between Case A* and Case A as a function of photovoltaic field area and H_2 storage duration: (**a**) global PTP efficiency, $RD_{\eta_{PTP}}$, and (**b**) annual electricity recovered by the PEMFC, $RD_{E_{PEMFC}}$.

As shown in Figure 12a, $RD_{\eta_{PTP}}$ remains mainly within approximately −2% to 6%. Figure 12b shows $RD_{E_{PEMFC}}$ values ranging approximately from −1% to 8%. The largest positive differences in both indicators occur predominantly at intermediate PV field areas and higher H_2 storage durations. The implications of these sensitivity results and their relation to the constant-efficiency assumption are discussed in Section 5.

5. Discussion

The comparison between Case A and Case B confirms the methodological limitation identified in the literature review: constant-efficiency representations can modify the predicted performance of PV-driven PTP systems when the AEL and PEMFC operate under temporal PV variability. In Case A, both conversion stages were represented through fixed efficiencies, following the simplified approach commonly used in system-level studies. Similar assumptions are reported in previous PTP and PTH_2 studies, where the electrolyzer is represented using fixed values such as 58% LHV [10], 61.5% [37], 68% [40], 70.5% for PEMEL [20], 72% for WEL [24], or 80% for AEL [22]. Fuel-cell reconversion is also frequently simplified, with constant values such as 40% [37], 46% [40], 47% [10], and 60% [45]. These values are useful for preliminary screening, but the results obtained in this work show that they can alter the annual energy balance, H_2 storage requirements, and electricity recovery of the complete PTP chain.

Table 8 shows that both cases supply the same annual electrical demand, E_{load} = 42.0 GWh yr^{-1}, and the same annual direct PV electricity, $E_{PV,direct}$ = 16.3 GWh yr^{-1}. Therefore, the main differences arise from the H_2 pathway. Although both cases use the same installed AEL capacity of 20.0 MW, Case A consumes 22.5 GWh yr^{-1} in the AEL and produces 4.40×10^5 kg yr^{-1} of H_2, whereas Case B consumes 7.5 GWh yr^{-1} and produces 1.46×10^5 kg yr^{-1}. This difference is caused by the way in which each model converts intermittent PV surplus into H_2. In Case A, the AEL is represented as a proportional energy-conversion block, so every unit of electricity assigned to electrolysis is converted into H_2 using a fixed LHV efficiency. In Case B, the quasi-dynamic AEL model links H_2 production to current density, cell voltage, Faraday efficiency, and thermal state; consequently, the effective SEC and the admissible operating points change with the instantaneous PV surplus. The lower mean AEL efficiency in Case B, $\overline{\eta}_{ely}$ = 0.551 instead of 0.650, together with the lower annual AEL electricity consumption, indicates that a smaller fraction of the available surplus is effectively converted and retained in the H_2 pathway. This lower H_2 availability propagates to the reconversion stage: E_{PEMFC} decreases from 6.3 to 2.4 GWh yr^{-1}, and the PEMFC operating time decreases from 1672.0 to 626.2 h yr^{-1}. As a result, SF_{PTP} decreases from 0.539 to 0.446, while $\eta_{global,PV-PTP}$ decreases from 0.529 to 0.440, corresponding to a relative difference of approximately 17% in the global efficiency indicator.

These renewable fractions quantify the contribution of the modeled PV–H_2 subsystem and should not be interpreted as complete electrical self-sufficiency of the Santa Cruz–Baltra system. The remaining annual demand is assigned to the background island electricity system, whose generation dispatch, fuel consumption, costs, and emissions are outside the scope of the present comparison.

The table also shows that the modeling approach affects the selected H_2 subsystem scale under the common design objective of maximizing renewable electricity coverage within the evaluated PV-area and H_2-storage design space. The quasi-dynamic case requires a smaller PEMFC capacity, 5.2 MW instead of 6.0 MW, and a smaller storage system, with $m_{H_2,tank,max}$ decreasing from 2334.3 to 903.6 kg and V_{tank} decreasing from 93.0 to 36.0 m^3. The required compressor capacity also decreases from 2327.8 to 712.7 kW. These results indicate that the effect of the modeling assumption is not limited to the instantaneous control response; it also modifies the annual H_2 inventory, reconversion requirements, and selected subsystem capacities. From a techno-economic perspective, this is relevant because LCOE depends simultaneously on the annualized cost numerator and the useful-energy denominator. Larger AEL, PEMFC, storage, and compressor requirements can increase CAPEX and OPEX, while higher H_2 production and higher E_{PEMFC} increase the amount of useful electricity over which those costs are distributed. Therefore, a constant-efficiency model can bias LCOE estimates by modifying both the required component scale and the apparent recovered

electricity. The final direction of this bias cannot be determined without a full cost model, but the present results show that the technical indicators entering an LCOE calculation are strongly affected by the efficiency-modeling approach.

The η_{PTP} and *SF* maps reinforce this interpretation. Case A produces a smoother and more regular response surface because the AEL and PEMFC behave as proportional conversion blocks. Thus, the relation between PV field area, H_2 storage hours, η_{PTP}, and *SF* is mainly governed by the energy balance and storage availability. This behavior is consistent with system-level formulations where the H_2 chain is modeled using fixed conversion efficiencies and dispatch constraints rather than electrochemical operating states [5,10,17,22,36,37]. In contrast, Case B produces a less regular contour structure, indicating that adding PV capacity does not necessarily translate into proportional useful electricity recovery when the AEL and PEMFC are represented through quasi-dynamic models.

Table 8. Selected component capacities and annual operational indicators for Case A, Case B and Case A*.

Indicator	Symbol	Case A	Case B	Case A*
Installed AEL capacity [MW]	$P_{AEL,installed}$	20.0	20.0	20.0
Installed PEMFC capacity [MW]	$P_{FC,installed}$	6.0	5.2	6.0
H_2 storage capacity [kg]	$m_{H_2,tank,max}$	2334.3	903.6	1932.7
Tank volume [m^3]	V_{tank}	93.0	36.0	77.0
Maximum tank pressure [bar]	p_{max}	350.0	350.0	350.0
Minimum annual tank pressure [bar]	$p_{tank,min}$	6.9	6.5	6.9
Maximum compressor power [kW]	$P_{comp,max}$	2327.8	712.7	1931.9
Annual electrical demand [GWh yr^{-1}]	E_{load}	42.0	42.0	42.0
Annual direct PV electricity [GWh yr^{-1}]	$E_{PV,direct}$	16.2	16.2	16.2
Annual PEMFC electricity [GWh yr^{-1}]	E_{PEMFC}	6.3	2.4	5.9
Annual AEL electricity consumption [GWh yr^{-1}]	E_{AEL}	22.5	7.5	22.31
Annual H_2 production [kg yr^{-1}]	$m_{H_2,year}$	439,564.1	145,525.1	368,808.6
AEL operating time [h yr^{-1}]	$t_{AEL,op}$	3159.8	3155.5	3152.6
PEMFC operating time [h yr^{-1}]	$t_{PEMFC,op}$	1672.0	626.2	1547.5
Mean AEL efficiency [-]	$\overline{\eta}_{ely}$	0.650	0.551	0.551
Mean PEMFC efficiency [-]	$\overline{\eta}_{FC}$	0.500	0.529	0.529
Minimum tank state of charge [-]	$SOC_{tank,min}$	0.02	0.02	0.02
Maximum tank state of charge [-]	$SOC_{tank,max}$	1.00	0.79	0.99
Mean tank state of charge [-]	$\overline{SOC}_{tank}$	0.54	0.25	0.46
Annual renewable fraction [-]	SF_{PTP}	0.539	0.446	0.526
Global PV-to-useful-load efficiency [-]	$\eta_{global,PV-PTP}$	0.529	0.440	0.520

Note: Case A corresponds to the constant-efficiency configuration, Case B corresponds to the quasi-dynamic AEL and PEMFC configuration, whereas Case A* corresponds to the constant efficiency configuration using the annual efficiencies obtained from Case B. $E_{PV,direct}$, E_{AEL}, E_{PEMFC}, E_{load}, and SF_{PTP} follow the annual definitions introduced in Section 3.7. The indicator $\eta_{global,PV-PTP}$ is defined here as $E_{REN,PTP}/E_{PV,gen}$ and should not be confused with the H_2 loop efficiency $\eta_{PTP} = E_{PEMFC}/(E_{AEL} + E_{aux})$.

The reason is that the conversion process is affected by the operating point of each device. For the AEL, U_{cell}, η_F, $\dot{V}_{H_2}$, T_{ely}, and SEC depend on current density, voltage losses, and thermal evolution, as described by the Ulleberg/TRNSYS Type 160 formulation [29,30]. For the PEMFC, V_{cell}, η_{FC}, and H_2 consumption depend on activation, ohmic, and concentration losses, as represented by the Amphlett–Mann model [25–28]. Therefore, the quasi-dynamic case captures component-level effects that are hidden in the constant-efficiency baseline.

The relative-difference maps quantify the magnitude of this effect over the full design space. The maximum $RD_{\eta_{PTP}}$ reached approximately 14%, concentrated around 10 ha of PV field area and approximately 4 h of H_2 storage. This value is within the same order of magnitude as previous findings showing that neglecting variable electrolyzer efficiency can overestimate H_2 production by 5–24% under renewable operation [33]. The effect was more

pronounced for E_{PEMFC}, where $RD_{E_{\mathrm{PEMFC}}}$ reached approximately 91% in regions with low H_2 storage hours and low PV field area. This result is consistent with the theoretical limitation discussed in the literature review: PEMFC units are often represented as aggregated H_2-to-electricity converters activated during deficit periods [5,10,11], although real PEMFC operation is governed by nonlinear voltage–current behavior.

These differences are relevant for techno-economic interpretation, even though no cost optimization is performed in this work. Previous studies use simplified H_2 subsystem efficiencies to size electrolyzers, fuel cells, storage systems, and renewable capacity [14,15,17,22,36]. If a constant-efficiency model overestimates E_{PEMFC}, H_2 production, or operating hours, it can also bias subsequent levelized indicators by modifying both the component scale and the useful-energy denominator. This may affect the estimated cost of produced H_2 and the apparent cost of recovered electricity, since larger AEL, PEMFC, compressor, and storage capacities increase CAPEX and OPEX, while higher useful output tends to reduce levelized costs.

Specifically, a 60%+ reduction in the recovered electricity, as observed under the quasi-dynamic formulation, substantially reduces the useful-energy denominator. From an energy planning perspective, previous sensitivity analyses on storage economics indicate that such a decrease in annual discharged energy could potentially double the apparent Levelized Cost of Storage (LCOS) for the reconverted electricity. As demonstrated in comparable LCOS assessments [67], reducing the utilization factor directly penalizes the economic viability, which could fundamentally alter optimal sizing limits and investment decisions for island microgrid deployments. The final direction of the bias depends on the cost structure, component sizing rule, and utilization level, which should be explicitly evaluated in future techno-economic work.

The present results should also be interpreted considering the input-data and operational simplifications adopted in the simulations. Because measured subhourly demand data for Santa Cruz–Baltra were not publicly available, the electric demand profile was synthetically generated from annual energy demand, monthly allocation, target peak demand, ambient-temperature modulation, and a representative intraday profile. Therefore, the absolute sizing results should be interpreted as case-study estimates constrained by these inputs rather than as a reproduction of measured feeder-level demand dynamics. Nevertheless, this approach provides a reproducible methodology for evaluating PV-driven PTP systems in locations where detailed load measurements are unavailable, because it can be implemented using planning indicators and meteorological records that are commonly available from official or public data sources. This limitation does not affect the internal comparison between Case A and Case B, since both configurations were evaluated using the same demand and PV inputs.

In addition, the model does not explicitly include equipment degradation, start-up and shut-down transients, minimum stable operating times, detailed ramp-rate constraints, storage leakage, pressure-regulation losses, water desalination and purification demands, or other site-specific operational restrictions that may affect commercial AEL-PEMFC operation.

Furthermore, the present simulations impose a minimum AEL operating load of 10% of nominal power for Cases A, A*, and B, as defined in Equation (50). This constraint accounts for the low-load operational limitations of alkaline electrolysis discussed in Section 3.7. Consequently, PV surplus below the prescribed operating threshold does not result in H_2 production. More detailed operational restrictions, including minimum stable operating times, equipment-specific start-up and shut-down sequences, ramp-rate constraints, and alternative standby strategies, are not explicitly resolved in the present system-level formulation and remain relevant extensions for future work.

These effects could further modify H_2 availability, PEMFC dispatch, component utilization, replacement schedules, CAPEX, OPEX, and levelized cost indicators. A further limitation concerns temporal resolution. The 6 min computational grid enables consistent chronological state propagation and system dispatch but does not reproduce meteorological fluctuations below the resolution of the original NSRDB data. Assessing such effects would require higher-frequency measurements or validated temporal-downscaling methods and is therefore beyond the scope of the present model-fidelity assessment. Therefore, future work should extend the proposed framework by using measured subhourly load records or stochastic demand ensembles, and by coupling the quasi-dynamic component models with degradation laws, detailed operational constraints, and cost models for both H_2 production and electricity recovery.

Compared with previous PTP studies, the contribution of this work is not the introduction of a new system architecture but the operational comparison between a constant-efficiency baseline and a quasi-dynamic model-based configuration. Studies such as Trapani et al. [10], He et al. [37], and Garner and Dehouche [40] demonstrate the role of H_2 storage in renewable systems, but these studies rely on fixed conversion efficiencies for one or both electrochemical components. Other studies incorporate more detailed or variable representations, such as electrochemical AEL models or piecewise efficiency curves for electrolyzer and fuel-cell behavior [30,31,41,42]. The present work extends this direction by linking validated low-order AEL and PEMFC models with commercial equipment data and evaluating their combined effect on H_2 production, storage utilization, electricity recovery, SF_{PTP}, η_{PTP}, and $\eta_{global,PV-PTP}$.

6. Conclusions

This study developed a system-level methodology for assessing PV–AEL–H_2–PEMFC power-to-power systems using catalog-informed component capacities and low-order physical models. The framework was applied to the Santa Cruz–Baltra case study using a 6 min temporal demand profile, PV generation, compressed H_2 storage, auxiliary compression, and a common supervisory-control structure. Two component representations were compared: Case A used fixed AEL and PEMFC conversion efficiencies, whereas Case B combined a quasi-dynamic AEL model with an operating-point-dependent PEMFC polarization model.

The AEL implementation reproduced the reference TRNSYS Type 160 voltage–current curves at 40, 60, and 80 °C, with $R^2 = 0.99904$, confirming the correct implementation of the reference formulation. A stack-specific calibration against the experimental data reported by Sánchez et al. reproduced the observed polarization behavior over the evaluated temperature, pressure, and current-density ranges. The PEMFC model also reproduced the experimental polarization trend, yielding an RMSE of 0.0123 V for the selected parameter combination, with the largest deviations occurring at high current density. These assessments support the use of the component models for comparative system simulations within the evaluated operating ranges, but they do not constitute validation of the complete annual PTP system.

The annual simulations showed that the selected component representation affects both the magnitude and spatial distribution of the performance indicators. Across most of the evaluated design space, increasing the PV field area and storage duration improved the renewable supply fraction, whereas the calculated efficiency of the hydrogen-storage loop generally decreased as a larger share of PV surplus was processed through the PTP pathway. The maximum relative difference in η_{PTP} was approximately 14%. The relative difference in E_{PEMFC} reached approximately 91% in low-PV-area and low-storage regions, where electricity recovery is highly sensitive to H_2 availability. This maximum relative value

should be interpreted cautiously because relative differences can be amplified when the recovered-electricity denominator is small.

For the representative configuration reported in Table 8, both cases were evaluated under the same annual electrical demand, $E_{load} = 42.0$ GWh yr^{-1}, and the same annual direct PV contribution, $E_{PV,direct} = 16.3$ GWh yr^{-1}. Case A produced 4.40×10^5 kg yr^{-1} of H_2 and recovered 6.3 GWh yr^{-1} through the PEMFC, whereas Case B produced 1.46×10^5 kg yr^{-1} and recovered 2.4 GWh yr^{-1}. Consequently, SF_{PTP} decreased from 0.539 to 0.446, while $\eta_{global,PV-PTP}$ decreased from 0.529 to 0.440, corresponding to a relative difference of approximately 17%. These results show that the selected component representation can materially affect the estimated renewable contribution and electricity recovery of the hydrogen pathway.

The reported renewable fractions should not be interpreted as complete island self-sufficiency. Demand not supplied by the modeled PV–H_2 subsystem remains assigned to the background island electricity system, whose dispatch, fuel consumption, cost, and emissions are outside the scope of the present assessment.

Under the adopted sizing procedure, Case B also resulted in lower selected PEMFC, H_2 storage, tank-volume, and compressor capacities, while the installed AEL capacity remained equal to 20.0 MW in both cases. These differences should be interpreted as model-dependent sizing outcomes rather than solely as differences in conversion efficiency, because the selected component capacities and the annual operating response are mutually coupled. A controlled comparison using identical subsystem capacities would be required to isolate exclusively the effect of component-model fidelity.

Overall, fixed-efficiency and operating-point-dependent representations can produce substantially different estimates of H_2 production, storage utilization, PEMFC dispatch, recovered electricity, and component sizing under temporal PV operation. Constant-efficiency models remain useful for preliminary screening and computationally intensive optimization, but the parameterization, energy basis, system boundaries, and associated uncertainty of these models should be reported explicitly. The present findings remain conditional on the synthetic demand profile, catalog-informed scaling procedure, storage assumptions, and simplified operational constraints. Future work should assess the framework using measured subhourly demand data and should incorporate equipment-specific start-up and shut-down behavior, minimum stable operating times, ramp-rate limitations, equipment degradation, storage losses, and techno-economic indicators for both H_2 production and recovered electricity.

Author Contributions: Conceptualization, A.V.-J.; Methodology, A.V.-J., S.R. and E.C.; Formal Analysis, A.V.-J., F.N., I.A., J.M.C., E.C., K.E.-S. and S.R.; Investigation, A.V.-J., E.C. and S.R.; Resources, S.R.; Writing—Original Draft Preparation, A.V.-J., S.R. and E.C.; Writing—Review and Editing, A.V.-J., F.N., I.A., J.M.C., E.C., K.E.-S. and S.R.; Visualization, A.V.-J.; Supervision, S.R.; Funding acquisition S.R. and E.C. All authors have read and agreed to the published version of the manuscript.

Funding: This research was funded by the Escuela Politécnica Nacional, grant number PIS-24-11. The APC was funded by the Escuela Politécnica Nacional.

Data Availability Statement: The original contributions presented in this study are included in the article. The meteorological inputs were derived from publicly available National Solar Radiation Database (NSRDB) data. Demand-planning information, commercial equipment data, and experimental validation data were obtained from the public sources cited in the manuscript. The synthetic demand profile and simulation results were generated using the equations, input parameters, assumptions, and figures reported in the article. No restricted, confidential, or proprietary datasets were used. Further inquiries can be directed to the corresponding author.

Acknowledgments: The authors gratefully acknowledge the financial support provided by Escuela Politécnica Nacional (EPN), the Departamento de Ingeniería Mecánica (DIM), and the PIS-24-11 project. J. M. Cardemil and I. Arias gratefully acknowledge the support from ANID/SERC Chile/CIN250043.

Conflicts of Interest: The authors declare no conflicts of interest.

Abbreviations

The following abbreviations and symbols are used in this manuscript:

AC	Alternating current	
AEL	Alkaline electrolyzer	
BESS	Battery energy storage system	
DC	Direct current	
DHI	Diffuse horizontal irradiance	[W m^{-2}]
DNI	Direct normal irradiance	[W m^{-2}]
FC	Fuel cell	
GHI	Global horizontal irradiance	[W m^{-2}]
H_2	Hydrogen	
HDKR	Hay–Davies–Klucher–Reindl	
LHV	Lower heating value	
NR	Not reported	
NSRDB	National Solar Radiation Database	
PEMEL	Proton-exchange membrane electrolyzer	
PEMFC	Proton-exchange membrane fuel cell	
PTP	Power-to-Power	
PTH_2	Power-to-Hydrogen	
PV	Photovoltaic	
RES	Renewable energy sources	
SEC	Specific electricity consumption	[kWh $kg_{H_2}^{-1}$]
SOC	State of charge	[%]
STD	Standard conditions	
E_{AEL}	Annual electricity consumed by the alkaline electrolyzer	[GWh]
E_{aux}	Annual auxiliary electricity consumption	[GWh]
E_{load}	Annual electrical demand	[GWh]
E_{PEMFC}	Annual electricity recovered by the fuel cell	[GWh]
$E_{PV,direct}$	Annual direct photovoltaic electricity supplied to load	[GWh]
$E_{REN,PTP}$	Annual renewable electricity supplied by the PTP system	[GWh]
$m_{H_2,year}$	Annual hydrogen production	[kg yr^{-1}]
SEC_{AEL}	AEL specific electricity consumption	[kWh $kg_{H_2}^{-1}$]
$m_{H_2,tank,max}$	Maximum hydrogen storage capacity	[kg]
P_{AEL}	Alkaline electrolyzer input power	[W]
$P_{AEL,installed}$	Installed alkaline electrolyzer capacity	[MW]
P_{bal}	Instantaneous renewable power balance	[W]
P_{comp}	Compressor electrical power	[W]
P_{def}	Power deficit to be supplied by the fuel cell	[W]
$P_{FC,installed}$	Installed fuel-cell capacity	[MW]
P_{load}	Electrical demand	[W]
P_{PEMFC}	Fuel-cell output power	[W]
$P_{PV,AC}$	Alternating-current photovoltaic power	[W]
P_{sur}	Surplus power available for hydrogen production	[W]
p_{tank}	Hydrogen tank pressure	[bar]
p_{max}	Maximum allowable storage pressure	[bar]
SF_{PTP}	Annual renewable fraction of the PTP system	[−]
SOC_{tank}	Hydrogen tank state of charge	[−]
V_{tank}	Hydrogen tank volume	[m^3]

$RD_{\eta_{PTP}}$	Relative difference in annual PTP efficiency	[%]
$RD_{E_{PEMFC}}$	Relative difference in annual fuel-cell electricity	[%]
η_{ely}	Alkaline electrolyzer efficiency	[%]
η_{FC}	Fuel-cell electrical efficiency	[%]
η_F	Faraday efficiency	[%]
$\eta_{global,PV-PTP}$	Global photovoltaic-to-useful-load efficiency	[%]
η_{PTP}	Net power-to-power efficiency of the hydrogen loop	[%]
$\overline{\eta}_{ely}$	Mean alkaline electrolyzer efficiency	[%]
$\overline{\eta}_{FC}$	Mean fuel-cell efficiency	[%]
$t_{AEL,op}$	Annual alkaline electrolyzer operating time	[h yr^{-1}]
$t_{PEMFC,op}$	Annual fuel-cell operating time	[h yr^{-1}]
$\dot{V}_{H_2}$	Hydrogen volumetric flow rate	[m^3 h^{-1}]
$\dot{V}_{H_2,AEL}$	Commercial-scale hydrogen production rate	[Nm^3 h^{-1}]
$\dot{V}_{H_2,N}$	Normal volumetric hydrogen flow rate	[Nm^3 h^{-1}]

Appendix A. Supplementary Tables

This appendix summarizes supplementary tabulated information used to support the component models and system-level simulations described in the main text. The tables include parameter sets, commercial equipment data, validation-specific inputs, and auxiliary assumptions required for model reproducibility. They are reported separately to keep the main methodology focused on the governing equations, model structure, and system-level coupling.

Table A1. Main technical parameters of the selected photovoltaic module from the CEC/SAM library [55].

Parameter	Value
Model	SEG-445-BMA-BG
Cell material	Mono-c-Si
Reference maximum power, $P_{mp,ref}$	445.12 W
Nominal efficiency, η_{PV}	23.80%
Module area, A_{mod}	1.87 m^2
Voltage at maximum power, $V_{mp,ref}$	41.60 V
Current at maximum power, $I_{mp,ref}$	10.70 A
Open-circuit voltage, $V_{oc,ref}$	49.90 V
Short-circuit current, $I_{sc,ref}$	11.34 A
Number of cells in series, N_s	72
Nominal operating cell temperature, T_{NOCT}	45.30 °C
Power temperature coefficient, γ_P	−0.384 %/°C

Table A2. Common literature-based and derived parameters used for commercial AEL scaling.

Parameter	Symbol	Value or Expression	Type	Source or Definition
Nominal current density	i_{nom}	280 mA/cm^2	L	[31]
Electrode area	A_e	0.25 m^2	L	[31]
Number of cells per stack	N_{cells}	21	L	[31]
Nominal Faraday efficiency	$\eta_{F,nom}$	0.96	L	[29,30]
Electrochemical coefficients	r_1, r_2, s_1, t_1, t_2, t_3, a_1, a_2	Type 160A reference set	L	[29,30]
Thermal resistance	R_T	0.167 K/W	L	[31]

Table A2. *Cont.*

Parameter	Symbol	Value or Expression	Type	Source or Definition
Thermal time constant	τ_T	29 h	L	[30]
Nominal stack current	$I_{stack,nom}$	$10 i_{nom} A_e$	D	Equation (19)
Series modules	$N_{ser,ely}$	$\frac{V_{dc}}{U_{stack,nom}}$	D	Equation (20)
Parallel branches	$N_{par,ely}$	$\frac{\dot{V}_{H_2,nom}}{N_{ser,ely}\dot{V}_{H_2,stack,nom}}$	D	Equation (21)
Equivalent stacks	N_{stacks}	$N_{ser,ely}N_{par,ely}$	D	Equation (22)
Nominal system current	I_{nom}	P_{nom}/V_{dc}	D	Equation (25)
Maximum current	I_{max}	$\gamma_I I_{nom}$	D	Equation (25)

Note: M = manufacturer catalog data, L = literature-based parameter, and D = derived parameter or modeling assumption. Manufacturer data are listed in Table 5. Literature-based parameters were taken from the alkaline electrolyzer formulation and reference values reported in [29,31,68]. Parameters classified as D were calculated from the scaling equations or assumed only for DC bus sensitivity analysis and commercial-scale integration.

Table A3. Base physical constants and electrochemical parameters used in the PEMFC model.

Parameter	Symbol	Value	Reference
Faraday constant	F	96,485 C mol^{-1}	Constant
Universal gas constant	R	8.3145 J mol^{-1} K^{-1}	Constant
Electrons per H_2 molecule	n	2	[28]
Hydrogen higher heating value	ΔH	2.86×10^5 J mol^{-1}	[28]
Thermoneutral voltage	U_{tn}	$\Delta H/(2F)$	[28]
Standard temperature	T_{STD}	0 °C	Constant
Standard pressure	p_{STD}	1 bar	Constant
Reference pressure	p_{ref}	1.01325 bar	[26]
Molar concentration at standard conditions	C_{STD}	$p_{STD}/(RT_{STD})$	Derived
Oxygen fraction in air	x_{O_2}	0.21	[28]
Active membrane area	A_{PEM}	48.79 cm^2	[60]
Membrane thickness	t_{PEM}	0.006 cm	Specification
Maximum current density	i_{max}	3000 mA cm^{-2}	[27]
Hydrogen stoichiometry	S_{H_2}	1.3	[60]
Air stoichiometry	S_{air}	2.5	[60]
Reference operating temperature	T_{design}	65 °C	[60]
Water transport coefficient	γ_w	0.0	[25]
Minimum cell voltage	V_{min}	0.30 V	[26]

Table A4. Fixed parameters adopted for the pressurized H_2 storage and auxiliary compressor models.

Parameter	Symbol	Value	Source
Universal gas constant	R	8.3145 J mol^{-1} K^{-1}	[61]
Reference pressure	p_{ref}	1.01325 bar	[61]
Reference temperature	T_{ref}	273.15 K	[61]
Hydrogen molar mass	M_{H_2}	2.016 g mol^{-1}	[61]
Hydrogen heat-capacity ratio	κ	1.41	[61]
Hydrogen critical temperature	T_{cr}	33.2 K	[61,63]
Hydrogen critical pressure	p_{cr}	12.8 bar	[61,63]
Compressor efficiency	η_{comp}	0.72	[63]
Maximum storage pressure	p_{max}	User-defined	Design input
Minimum tank state of charge	SOC_{min}	User-defined	Design input
Target tank state of charge	SOC_{target}	User-defined	Design input

Appendix B. Auxiliary Hydrogen Storage and Compression Definitions

This appendix reports auxiliary relations used by the hydrogen storage and auxiliary compression model described in Section 3.6.

The molar H_2 flow associated with a normal volumetric flow rate ($\dot{n}_{H_2}$) was calculated as

$$\dot{n}_{H_2} = \dot{V}_{H_2,N} \frac{p_{ref}}{RT_{ref}} \tag{A1}$$

where $\dot{V}_{H_2,N}$ is the normal volumetric H_2 flow rate, p_{ref} is the reference pressure, R is the universal gas constant, and T_{ref} is the reference temperature.

The van der Waals constants (a and b) used in Equation (44) were calculated from the critical properties of H_2 as

$$a = \frac{27R^2T_{cr}^2}{64p_{cr}}, \qquad b = \frac{RT_{cr}}{8p_{cr}} \tag{A2}$$

where T_{cr} is the critical temperature of H_2 and p_{cr} is the critical pressure of H_2.

The required normal H_2 volume for storage sizing ($V_{need,N}$) and the maximum normal H_2 volume stored in a candidate tank ($V_{gas,max,N}$) were estimated as

$$V_{need,N} = \frac{V_{day,target,N}}{SOC_{target}}, \qquad V_{gas,max,N} = \frac{p_{max}}{p_{ref}} \frac{T_{ref}}{T_{gas,max}} V_{tank} \tag{A3}$$

where $V_{day,target,N}$ is the target daily H_2 demand at normal conditions, SOC_{target} is the desired maximum operating pressure fraction, and $T_{gas,max}$ is the maximum gas temperature considered during pre-sizing. The selected tank volume was the smallest candidate satisfying

$$V_{gas,max,N} \geq V_{need,N} \tag{A4}$$

This criterion sizes the tank from the required daily autonomy while avoiding unnecessary oversizing.

The H_2 inflow to the tank ($\dot{V}^k_{H_2,in}$) and the H_2 outflow from the tank ($\dot{V}^k_{H_2,out}$) were governed by the renewable power balance:

$$\dot{V}^k_{H_2,in} > 0 \quad \text{if} \quad P^k_{sur} > 0, \qquad \dot{V}^k_{H_2,out} > 0 \quad \text{if} \quad P^k_{def} > 0 \text{ and } SOC^k_{tank} > SOC_{min} \tag{A5}$$

where P^k_{sur} is the renewable power surplus, P^k_{def} is the unmet electrical demand, and SOC_{min} is the minimum allowable tank state of charge. Therefore, surplus renewable electricity is converted into H_2 and stored, whereas stored H_2 is reconverted into electricity by the PEMFC during deficit periods.

References

1. Zurita, A.; Mata-Torres, C.; Cardemil, J.M.; Guédez, R.; Escobar, R.A. Multi-objective optimal design of solar power plants with storage systems according to dispatch strategy. *Energy* **2021**, *237*, 121627. [CrossRef]
2. Vega-Garita, V.; Sofyan, M.F.; Narayan, N.; Ramirez-Elizondo, L.; Bauer, P. Energy Management System for the Photovoltaic Battery Integrated Module. *Energies* **2018**, *11*, 3371. [CrossRef]
3. Grisales-Noreña, L.F.; Ramos-Paja, C.A.; Gonzalez-Montoya, D.; Alcalá, G.; Hernandez-Escobedo, Q. Energy Management in PV Based Microgrids Designed for the Universidad Nacional de Colombia. *Sustainability* **2020**, *12*, 1219. [CrossRef]
4. Osmani, K.; Haddad, A.; Alkhedher, M.; Lemenand, T.; Castanier, B.; Ramadan, M. A Novel MPPT-Based Lithium-Ion Battery Solar Charger for Operation under Fluctuating Irradiance Conditions. *Sustainability* **2023**, *15*, 9839. [CrossRef]
5. Superchi, F.; Bianchini, A.; Moustakis, A.; Pechlivanoglou, G. Towards sustainable energy independence: A case study of green hydrogen as seasonal storage integration in a small island. *Renew. Energy* **2025**, *245*, 122813. [CrossRef]
6. Mohamed, Y.A.; Zobaa, A.M.; Ibrahim, A.M.; Boghdady, T.A. Towards a fully sustainable UPQC-DG system: Combining PV, fuel cells, BESS, water Electrolyzer and green hydrogen storage through a novel power management approach. *J. Energy Storage* **2025**, *113*, 115653. [CrossRef]
7. Nieto, F.; de la Calle, A.; Arias, I.; Cardemil, J.M.; Bayon, A.; Escobar, R. Annual performance of a calcium looping thermochemical energy storage with sCO2 Brayton cycle in a solar power tower. *Energy* **2025**, *336*, 138344. [CrossRef]

8. Escamilla, A.; Sánchez, D.; García-Rodríguez, L. Assessment of power-to-power renewable energy storage based on the smart integration of hydrogen and micro gas turbine technologies. *Int. J. Hydrogen Energy* **2022**, *47*, 17505–17525. [CrossRef]
9. Buffo, G.; Marocco, P.; Ferrero, D.; Lanzini, A.; Santarelli, M. Chapter 15-Power-to-X and power-to-power routes. In *Solar Hydrogen Production*; Calise, F., D'Accadia, M.D., Santarelli, M., Lanzini, A., Ferrero, D., Eds.; Academic Press: Cambridge, MA, USA, 2019 ; pp. 529–557. [CrossRef]
10. Trapani, D.; Marocco, P.; Ferrero, D.; Lindberg, K.B.; Sundseth, K.; Santarelli, M. The potential of hydrogen-battery storage systems for a sustainable renewable-based electrification of remote islands in Norway. *J. Energy Storage* **2024**, *75*, 109482. [CrossRef]
11. Williams, L.; Wang, Y. A distributed renewable power system with hydrogen generation and storage for an island. *Appl. Energy* **2024**, *358*, 122500. [CrossRef]
12. Covelli, D.; Virgüez, E.; Caldeira, K.; Lewis, N.S. Oahu as a case study for island electricity systems relying on wind and solar generation instead of imported petroleum fuels. *Appl. Energy* **2024**, *375*, 124054. [CrossRef]
13. Mühlbauer, A.; Fan, Y.F.; Sambor, D.J.; Jacobson, M.Z. Minimizing the multi-decadal cost of islanded renewable-electricity microgrids for different climate zones. *Smart Energy* **2025**, *20*, 100208. [CrossRef]
14. Mai, T.M.; Cristofari, C.; Azzaro-Pantel, C.; Carrera, E. Renewable hydrogen supply chain for transport application in Corsica island. In *Computer Aided Chemical Engineering*; Elsevier B.V.: Amsterdam, The Netherlands, 2022; Volume 51, pp. 895–900. [CrossRef]
15. Mai, T.M.; Azzaro-Pantel, C.; Cristofari, C.; Choi, M.C. A prospective approach to the optimal deployment of a hydrogen supply chain for sustainable mobility in island territories: Application to Corsica. *Int. J. Hydrogen Energy* **2024**, *93*, 975–991. [CrossRef]
16. Montignac, F.; Chavez, D.L.; Arpajou, M.C.; Ruby, A. Assessment of hydrogen supply chains based on dynamic bi-objective optimization of costs and greenhouse gases emissions: Case study in the context of Balearic Islands. *Energy* **2024**, *308*, 132590. [CrossRef]
17. Nami, H.; Ardehali, A.; Wenzel, H. Optimal sizing of electrolysis systems in regions with renewable energy and limited transmission capacity: A case study of the Lolland-Falster islands, Denmark. *Energy* **2025**, *328*, 136584. [CrossRef]
18. Choi, J.; Eom, D.; Park, B.; Song, J.; Kook, M.; Park, S. Clean energy supply and demand strategies of Jeju Island to achieve carbon net-zero by using digital twin technology. *Energy* **2025**, *314*, 134178. [CrossRef]
19. Rivera, Y.; Berna-Escriche, C.; Córdova-Chávez, Y.; Álvarez Piñeiro, L.; Blanco, D. Forecasts for full decarbonization of the economy in off-grid systems with high end-use consumption rates through combined electricity and hydrogen deployment, the Canary Islands in 2040. *J. Energy Storage* **2025**, *114*, 115912. [CrossRef]
20. Berna-Escriche, C.; Rivera-Durán, Y.; Córdova-Chávez, Y.; Muñoz-Cobo, J.L. Maximizing the use of hydrogen as energy vector to cover the final energy demand for stand-alone systems, application and sensitivity analysis for the Canary Archipelago by 2040. *Prog. Nucl. Energy* **2023**, *163*, 104791. [CrossRef]
21. Berna-Escriche, C.; Blanco, D.; Rivera, Y.; Álvarez Piñeiro, L.; Muñoz-Cobo, J.L. Performance of renewable systems hybridized with the most promising SMR designs for the full economy decarbonization using hydrogen and electricity for standalone systems, the Canary Islands in 2040. *Sustain. Energy Technol. Assess.* **2025**, *74*, 104199. [CrossRef]
22. Hajjaji, M.; Cristofari, C. Economic and technical evaluation of on-site electrolysis solar hydrogen refueling station in Corsica: A case study of Ajaccio. *Renew. Energy* **2024**, *231*, 120982. [CrossRef]
23. Andreae, E.; Petersen, M.; Skov, I.R.; Nielsen, F.D.; You, S.; Bindner, H.W. The impact of offshore energy hub and hydrogen integration on the Faroe Island's energy system. *Smart Energy* **2024**, *16*, 100161. [CrossRef]
24. Salmelin, M.; Hyypiä, J.; Satymov, R.; Galimova, T.; Talus, K.; Karjunen, H.; Lassila, J.; Breyer, C. Exploring the Shetland Islands' potential as a green e-hydrogen export hub for Europe. *Energy* **2025**, *339*, 138682. [CrossRef]
25. Amphlett, J.C.; Baumert, R.M.; Mann, R.F.; Peppley, B.A.; Roberge, P.R.; Harris, T.J. Performance Modeling of the Ballard Mark IV Solid Polymer Electrolyte Fuel Cell: I. Mechanistic Model Development. *J. Electrochem. Soc.* **1995**, *142*, 1–8. [CrossRef]
26. Mann, R.F.; Amphlett, J.C.; Hooper, M.A.; Jensen, H.M.; Peppley, B.A.; Roberge, P.R. Development and application of a generalised steady-state electrochemical model for a PEM fuel cell. *J. Power Sources* **2000**, *86*, 173–180. [CrossRef]
27. Correa, J.; Farret, F.; Canha, L.; Simoes, M. An electrochemical-based fuel-cell model suitable for electrical engineering automation approach. *IEEE Trans. Ind. Electron.* **2004**, *51*, 1103–1112. [CrossRef]
28. O'Hayre, R.; Cha, S.W.; Colella, W.; Prinz, F.B. *Fuel Cell Fundamentals*, 3rd ed.; John Wiley & Sons: Hoboken, NJ, USA, 2016.
29. Ulleberg, Ø. Modeling of advanced alkaline electrolyzers: A system simulation approach. *Int. J. Hydrogen Energy* **2003**, *28*, 21–33. [CrossRef]
30. Solar Energy Laboratory, University of Wisconsin–Madison. *TRNSYS 17: A Transient System Simulation Program, Volume 4: Mathematical Reference*; Section 4.5.3, Type 160: Advanced Alkaline Electrolyzer; Solar Energy Laboratory, University of Wisconsin–Madison: Madison, WI, USA, 2014; pp. 4–156–4–161. Available online: http://trnsys.org/MaillistArchive/pdfkSLYr_lzDr.pdf (accessed on 28 March 2026)
31. Karacavus, B.; Aydın, K. Hydrogen production and storage analysis of a system by using TRNSYS. *Int. J. Hydrogen Energy* **2020**, *45*, 34608–34619. [CrossRef]

32. Yang, J.; Zhang, J.; Liu, M.; Sun, J.; Shangguan, Z. Dynamic Simulation and Performance Analysis of Alkaline Water Electrolyzers for Renewable Energy-Powered Hydrogen Production. *Energies* **2024**, *17*, 4915. [CrossRef]
33. Virah-Sawmy, D.; Beck, F.J.; Sturmberg, B. Ignore variability, overestimate hydrogen production–Quantifying the effects of electrolyzer efficiency curves on hydrogen production from renewable energy sources. *Int. J. Hydrogen Energy* **2024**, *72*, 49–59. [CrossRef]
34. Martinez Lopez, V.; Ziar, H.; Haverkort, J.; Zeman, M.; Isabella, O. Dynamic operation of water electrolyzers: A review for applications in photovoltaic systems integration. *Renew. Sustain. Energy Rev.* **2023**, *182*, 113407. [CrossRef]
35. Le Bideau, D.; Chocron, O.; Mandin, P.; Kiener, P.; Benbouzid, M.; Sellier, M.; Kim, M.; Ganci, F.; Inguanta, R. Evolutionary Design Optimization of an Alkaline Water Electrolysis Cell for Hydrogen Production. *Appl. Sci.* **2020**, *10*, 8425. [CrossRef]
36. Pompodakis, E.E.; Ahmed, A.; Condaxakis, C.; Orfanoudakis, G.I.; Karapidakis, E.S. Paving the way toward hydrogen mobility: An effective policy to reduce the green hydrogen cost. *Int. J. Hydrogen Energy* **2025**, *100*, 417–427. [CrossRef]
37. He, H.; Huang, Y.; Nakadomari, A.; Masrur, H.; Krishnan, N.; Hemeida, A.M.; Mikhaylov, A.; Senjyu, T. Potential and economic viability of green hydrogen production from seawater electrolysis using renewable energy in remote Japanese islands. *Renew. Energy* **2023**, *202*, 1436–1447. [CrossRef]
38. Gao, J.; Wu, H.; Gao, F.; Huang, N.; Tan, Q. Hydrogen utilization planning for island integrated system considering uncertainties of both source and load sides. *J. Clean. Prod.* **2025**, *515*, 145815. [CrossRef]
39. Nasser, M.; Megahed, T.F.; Ookawara, S.; Hassan, H. Techno-economic assessment of clean hydrogen production and storage using hybrid renewable energy system of PV/Wind under different climatic conditions. *Sustain. Energy Technol. Assess.* **2022**, *52*, 102195. [CrossRef]
40. Garner, R.; Dehouche, Z. Optimal Design and Analysis of a Hybrid Hydrogen Energy Storage System for an Island-Based Renewable Energy Community. *Energies* **2023**, *16*, 7363. [CrossRef]
41. Marocco, P.; Ferrero, D.; Martelli, E.; Santarelli, M.; Lanzini, A. An MILP approach for the optimal design of renewable battery-hydrogen energy systems for off-grid insular communities. *Energy Convers. Manag.* **2021**, *245*, 114564. [CrossRef]
42. Marocco, P.; Ferrero, D.; Lanzini, A.; Santarelli, M. The role of hydrogen in the optimal design of off-grid hybrid renewable energy systems. *J. Energy Storage* **2022**, *46*, 103893. [CrossRef]
43. Hassan, Q.; Abdulrahman, I.S.; Salman, H.M.; Olapade, O.T.; Jaszczur, M. Techno-Economic Assessment of Green Hydrogen Production by an Off-Grid Photovoltaic Energy System. *Energies* **2023**, *16*, 744. [CrossRef]
44. Qiu, C.; Wen, Z.; He, G.; Zhang, K.; Xu, Z. Optimal Sizing of Power and Hydrogen Storage Systems Considering Electrolyzer Efficiency and Start-Up Dynamics. *Energies* **2026**, *19*, 1712. [CrossRef]
45. Hidouri, D.; Ben Omrane, I.; Khalil, K.; Cherif, A. Energy Management of a 1 MW Photovoltaic Power-to-Electricity and Power-to-Gas for Green Hydrogen Storage Station. *World Electr. Veh. J.* **2025**, *16*, 227. [CrossRef]
46. Llerena-Pizarro, O.R.; Micena, R.P.; Tuna, C.E.; Silveira, J.L. Electricity sector in the Galapagos Islands: Current status, renewable sources, and hybrid power generation system proposal. *Renew. Sustain. Energy Rev.* **2019**, *108*, 65–75. [CrossRef]
47. Ministerio de Energía y Minas del Ecuador. *Plan de Transición Energética de las Islas Galápagos: Evolución Energética*; Ministry of Energy and Mines: Quito, Ecuador, 2023.
48. Córdova Villagómez, J.J.; Constante, G.; Cabrera, G. Análisis de la Dependencia Anual de la Demanda de Energía Eléctrica Frente a la Temperatura Ambiente. *Rev. PolitécNica* **2014**, *33*. Available online: https://revistapolitecnica.epn.edu.ec/ojs2/index.php/revista_politecnica2/article/view/163 (accessed on 21 December 2025).
49. The MathWorks Inc. *MATLAB Version: 24.2 (R2024b) Update 1*; The MathWorks Inc.: Natick, MA, USA, 2024.
50. National Renewable Energy Laboratory. NSRDB: National Solar Radiation Database US Data. Available online: https://nsrdb.nlr.gov/data-viewer (accessed on 19 June 2023).
51. Duffie, J.A.; Beckman, W.A. *Solar Engineering of Thermal Processes*, 4th ed.; John Wiley and Sons, Ltd.: Hoboken, NJ, USA, 2013. [CrossRef]
52. De Soto, W.; Klein, S.; Beckman, W. Improvement and validation of a model for photovoltaic array performance. *Solar Energy* **2006**, *80*, 78–88. [CrossRef]
53. King, D.L.; Boyson, W.E.; Kratochvi, J.A., II. *Photovoltaic Array Performance Model*; Technical Report; SANDIA National Laboratories: Albuquerque, NM, USA, 2004. Available online: https://pvpmc.sandia.gov/modeling-guide/2-dc-module-iv/point-value-models/sandia-pv-array-performance-model/ (accessed on 2 June 2025).
54. Villarruel-Jaramillo, A.; Rosales-Pérez, J.F.; Pérez-García, M.; Cardemil, J.M.; Escobar, R. Modeling and Performance Evaluation of Hybrid Solar Cooling Systems Driven by Photovoltaic and Solar Thermal Collectorsmdash; Case Study: Greenhouses of Andalusia. *Energies* **2023**, *16*, 4888. [CrossRef]
55. National Renewable Energy Laboratory; Golden, C. System Advisor Model Version 2020.11.29 (SAM 2020.11.29). Available online: https://sam.nlr.gov/download/version-2021-12-01.html (accessed on 3 February 2026).

56. Aguado, R.; Baccioli, A.; Liponi, A.; Vera, D. Continuous decentralized hydrogen production through alkaline water electrolysis powered by an oxygen-enriched air integrated biomass gasification combined cycle. *Energy Convers. Manag.* **2023**, *289*, 117149. [CrossRef]
57. Ju, S.; Cai, M.; Shakaraliyeva, Z.; Umarova, N.; Li, F. Energy management and efficiency evaluation of an integrated off-grid hydrogen energy use system. *Energy Strategy Rev.* **2026**, *64*, 102078. [CrossRef]
58. HFSinoPower. Alkaline Water Electrolysis Hydrogen Production Equipment. Available online: https://www.hfsinopower.com/5nm3h-25kw-alk-hydrogen-electrolyzer-stack-water-electrolysis (accessed on 13 July 2026).
59. Verde Hydrogen. VERDE Electrolyzer- Products. Available online: https://verdehydrogen.com/verde-100-electrolyser (accessed on 13 July 2026).
60. Suárez, C.; Iranzo, A.; Toharias, B.; Rosa, F. Experimental and numerical Investigation on the design of a bioinspired PEM fuel cell. *Energy* **2022**, *257*, 124799. [CrossRef]
61. Çengel, Y.A.; Boles, M.A. *Thermodynamics: An Engineering Approach*, 8th ed.; McGraw-Hill Education: New York, NY, USA, 2015.
62. Ulleberg, Ø. Stand-Alone Power Systems for the Future: Optimal Design, Operation & Control of Solar-Hydrogen Energy Systems. Ph.D. Thesis, Norwegian University of Science and Technology, Trondheim, Norway, 1998.
63. Barthélémy, H.; Weber, M.; Barbier, F. Hydrogen storage: Recent improvements and industrial perspectives. *Int. J. Hydrogen Energy* **2017**, *42*, 7254–7262. [CrossRef]
64. de Groot, M.T.; Kraakman, J.; Garcia Barros, R.L. Optimal operating parameters for advanced alkaline water electrolysis. *Int. J. Hydrogen Energy* **2022**, *47*, 34773–34783. [CrossRef]
65. Haoran, C.; Xia, Y.; Wei, W.; Yongzhi, Z.; Bo, Z.; Leiqi, Z. Safety and efficiency problems of hydrogen production from alkaline water electrolyzers driven by renewable energy sources. *Int. J. Hydrogen Energy* **2024**, *54*, 700–712. [CrossRef]
66. Sánchez, M.; Amores, E.; Rodríguez, L.; Clemente-Jul, C. Semi-empirical model and experimental validation for the performance evaluation of a 15 kW alkaline water electrolyzer. *Int. J. Hydrogen Energy* **2018**, *43*, 20332–20345. [CrossRef]
67. Jülch, V. Comparison of electricity storage options using levelized cost of storage (LCOS) method. *Appl. Energy* **2016**, *183*, 1594–1606. [CrossRef]
68. TRNSYS. TRNSYS: Transient System Simulation Tool. Available online: http://www.trnsys.com/ (accessed on 28 March 2026).

Disclaimer/Publisher's Note: The statements, opinions and data contained in all publications are solely those of the individual author(s) and contributor(s) and not of MDPI and/or the editor(s). MDPI and/or the editor(s) disclaim responsibility for any injury to people or property resulting from any ideas, methods, instructions or products referred to in the content.